

# Australia Telescope Compact Array Survey of Candidate Ultra-Compact and Buried HII Regions in the Magellanic Clouds

Rémy Indebetouw, Kelsey E. Johnson

*University of Wisconsin Astronomy Department, 475 N. Charter St., Madison, WI 53705  
(remy@astro.wisc.edu, kjohnson@astro.wisc.edu)*

and

Peter Conti

*JILA, University of Colorado, 440-UCB, Boulder, CO, 80309 (pconti@jila.colorado.edu)*

## ABSTRACT

We present a systematic survey for ultracompact H II (UCH II) regions in the Magellanic Clouds. Understanding the physics of massive star formation (MSF) is a critical astrophysical problem. The study of MSF began in our galaxy with surveys of UCH II regions, but before now this has not been done for other galaxies. We selected candidates based on their Infrared Astronomical Satellite (IRAS) colors and imaged them at 3 and 6 cm with the Australia Telescope Compact Array (ATCA). Nearly all of the observed regions contain compact radio sources consistent with thermal emission. Many of the sources are related to optically visible H II regions, and often the radio emission traces the youngest and densest part of the H II region. The luminosity function and number distribution of Lyman continuum fluxes of the compact radio sources are consistent with standard stellar and cluster initial mass functions. This type of systematic assessment of IRAS diagnostics is important for interpreting *Spitzer* Space Telescope data, which will probe similar physical scales in nearby galaxies as IRAS did in the Magellanic Clouds.

*Subject headings:* stars: formation — HII regions — Magellanic Clouds

## 1. Introduction

Massive stars play a major role in the dynamical evolution of galaxies: they are responsible for the ionization of the interstellar medium, their stellar winds and supernovae are

dominant sources of mechanical energy, their ultraviolet radiation powers far-infrared luminosities through the heating of dust, and they are a main driver of chemical evolution in the universe via supernova explosions at the end of their lives. However, despite the significant role of massive stars throughout the universe, their birth is not well understood, and we are only beginning to piece together a scenario for the youngest stages of massive star evolution. We have made some progress understanding the early stages of massive star formation in the Galaxy, but the current knowledge about the early stages of massive star evolution in other environments is mediocre at best.

The reasons for this dearth of information about extremely young massive stars in other galaxies are predominantly twofold: (1) the earliest stages of massive star evolution are deeply enshrouded and inaccessible in the optical and near-infrared regimes; and (2) high spatial resolutions are necessary to disentangle the individual massive stars from their surrounding environment and background contamination. Radio observations using the Australia Telescope Compact Array (ATCA) are uniquely capable of overcoming these obstacles for the galaxies nearest to our own, the Large and Small Magellanic Clouds. Synthesis imaging observations at centimeter wavelengths are sensitive to the free-free emission emitted by the densest compact ionized regions, and the centimeter spectral index can be used to differentiate those extremely dense regions suffering from self-absorption.

We have conducted a survey of candidate UCH II regions in the Magellanic Clouds with high (1–2'') spatial resolution at 3 and 6 cm using the ATCA. Section 2 contains a description of the FIR-based candidate selection, the radio observing strategy, data reduction, and lists the detected sources. Individual compact H II regions with interesting radio morphologies are described in the Appendix, and the statistical properties of the population as a whole are analyzed in section 3.

## 2. Observations

### 2.1. Far Infrared Target Selection

One goal of this project was to test the effectiveness of using far-infrared (FIR) colors at fairly low spatial resolution to discover massive protostellar objects. This exercise using IRAS data in the Magellanic Clouds is particularly interesting because the *Spitzer* Space Telescope probes similar spatial scales in nearby galaxies as IRAS did in the Magellanic Clouds.

The primary target selection criterion for this survey was thus FIR color. Wood & Churchwell (1989b, hereafter WC89) determined that the majority of Galactic ultra-compact

H II (UCH II) regions have particular mid- to far-infrared colors which distinguish them from other astronomical objects. They indicated (their Figure 1b) that most sources with IRAS colors  $F_\nu(60\mu m)/F_\nu(12\mu m) \geq 20$ . and  $F_\nu(25\mu m)/F_\nu(12\mu m) \geq 3.7$  are UCH II s (these colors correspond to black-body temperatures  $\lesssim 105$  and  $\lesssim 160$  K, respectively). More importantly in the context of this work, they found that there was little color contamination – compared to a random selection of Galactic IRAS sources, most of the objects in that region of color-color space were UCH II regions.

To exploit this fact, we first combined the IRAS point source catalog with a multi-wavelength Parkes radio continuum survey (Filipović, Haynes, White, & Jones 1998, and references therein). The Parkes surveys have a resolution of 2.8 arcmin at 8.55 GHz (which corresponds to a linear distance of  $\sim 49$  pc in the SMC and  $\sim 41$  pc in the LMC), so we took as a match to each radio source the brightest IRAS source within 2.5 arcminutes. We then examined the FIR to radio spectral energy distribution of all the objects with slightly broader colors than the WC89 criteria:  $F_{24\mu m}/F_{12\mu m} > 1$  and  $F_{60\mu m}/F_{12\mu m} > 10$ . This sample contained 98 objects in the LMC (47 with the stricter WC89 colors) and 22 in the SMC (8 with WC89 colors). Finally, we chose those targets which were consistent with having flat or inverted radio emission at  $\lambda \sim 1\text{--}5$  cm. Thus our sample is FIR-color selected, but objects which are highly nonthermal at cm wavelengths at the resolution of the Parkes survey are excluded. This last criterion was imposed to bias against supernova remnants and other sources of nonthermal emission. Sources consistent with optically thin thermal emission (slightly negative spectral index  $\alpha \sim -0.1$  where  $F_\nu \propto \nu^\alpha$ ) were kept as candidates under the presumption that H II regions observed at low resolution will be dominated by the optically thin envelopes, but may still contain compact, more optically thick sources. Figure 1 shows our target objects in an IRAS color-color space identical to that of WC89’s Figure 1b. The two targets which fall farthest outside of the color selection box were cases for which the IRAS flux densities or identification were ambiguous.

## 2.2. Radio Observations and Data Reduction

Candidate fields were observed with the ATCA during two runs in May 2001 and May 2002. Simultaneous observations were obtained at 3 cm (8.6 GHz) and 6 cm (4.8 GHz) in the highest resolution configurations (6F in 2001, 6A in 2002). Each field was observed for roughly 3 hours, with some time added for a few of the faintest fields. We observed 19 of the 29 selected fields in the LMC, and 7 of the 8 selected fields in the SMC. For some of the fields, archival data was available, which allowed compact sources to be tabulated for 3 additional candidates. Our observations are summarized in Table 1, and the archival

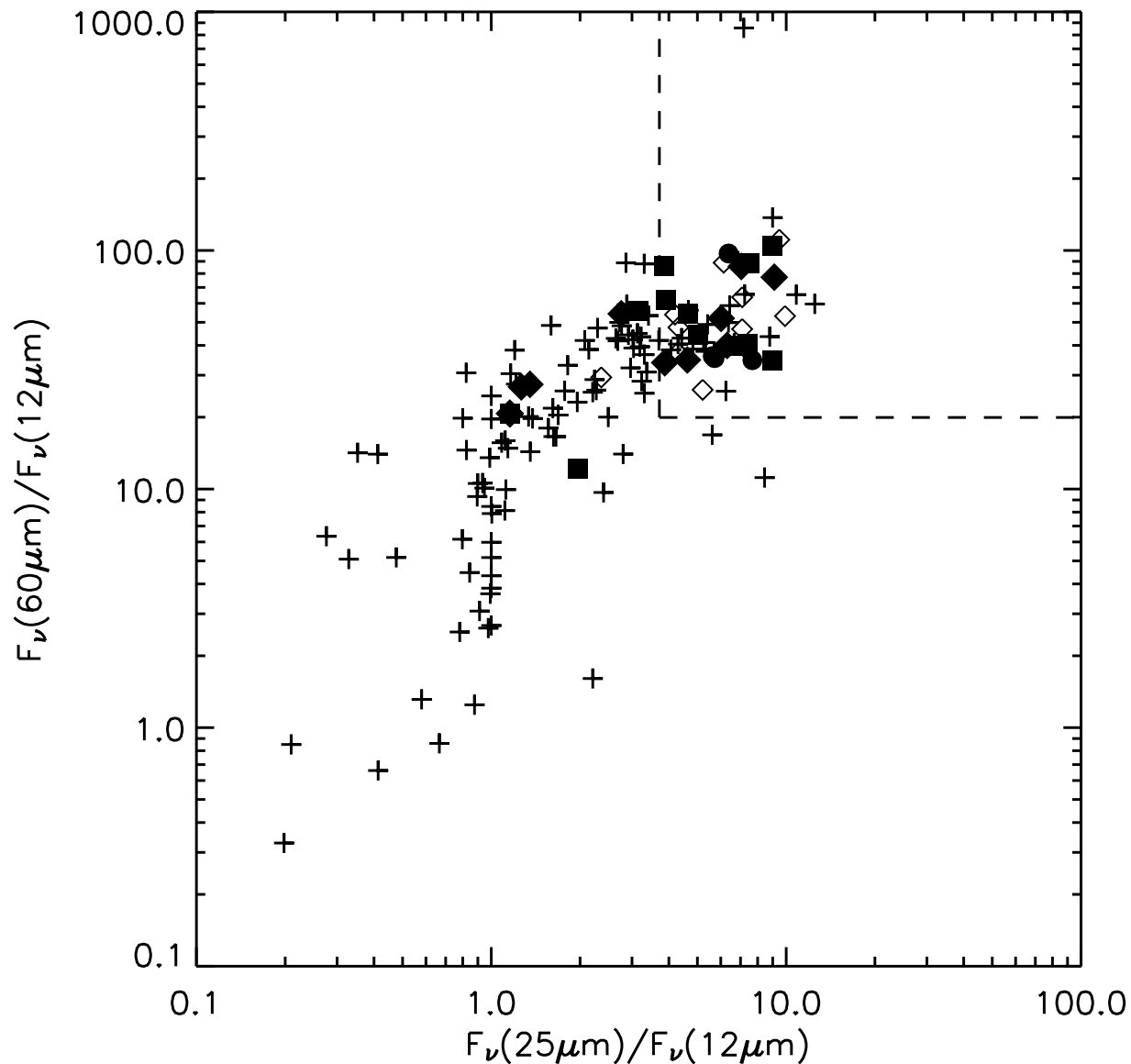


Fig. 1.— Candidate UCH II regions in the Magellanic Clouds. All IRAS sources with Parkes radio detections in the Clouds are marked (crosses), our candidates in bold symbols (filled diamonds observed 5/2001, squares observed 5/2002, filled circles existing archival observations). The color selection box of WC89 is marked; we used a slightly relaxed color selection criterion in order to test the validity of that box at the lower spatial resolution available in the Magellanic Clouds.

observations which we completely re-reduced for consistency, are summarized in Table 2.

The receivers simultaneously detect 4800 MHz ( $\sim 6$  cm) and 8640 MHz ( $\sim 3$  cm), with primary beams (field of view) of 10 and 5 arcminutes, respectively. Each frequency had a bandwidth of 128 MHz, and the resulting theoretical RMS noise for these observations is  $\approx 0.07$  mJy/beam. The absolute flux density scale was determined by assuming a flux density for PKS1934-638 of 5.83 Jy at 4.8 GHz and 2.84 at 8.6 GHz, and we estimate that the resulting flux density scale is uncertain by less than  $\sim 5\%$ .

Calibration was carried out using the Miriad data reduction package, including gain, phase, and polarization calibrations of the flux density calibrator and phase calibrators. Following the calibration, data were loaded into the Astronomical Image Processing System (AIPS) where they were inverted and cleaned using the task IMAGR. In order to optimize the synthesized beam at 4.8 GHz, a fairly uniform weighting was used (robust=0), while a more natural weighting was used at 8.6 GHz (robust=3) in order to increase the sensitivity. In addition, the  $uv$  range of the 4.8 GHz data was limited in order to better match the shortest  $uv$  coverage of the 8.6 GHz data. It should be noted that this does not create matched beams at 3cm and 6cm, but simply mitigates the influence of extended structure at 6cm; the 6cm observations still have denser  $uv$  coverage at short spacings, and the 3cm observations still have  $uv$  coverage at long spacings not available in the 6cm observations. Based on the resulting  $uv$  coverage, the largest angular scales to which these data are sensitive are  $\lesssim 30''$  at 6 cm and  $\lesssim 20''$  at 3 cm. The images at both frequencies were then corrected for the primary beam sensitivity.

Radio flux densities were measured in AIPS++ using two methods. The first method used the VIEWER program to place identical apertures around the 3 cm and 6 cm images, and background levels were estimated using surrounding annuli. Several combinations of apertures and annuli were used in order to estimate the uncertainty in the flux density. The second method used the IMAGEFITTER to fit two-dimensional Gaussians to the sources. Final flux densities were determined by averaging these results, and the uncertainties were determined from the scatter of these results in combination with the uncertainty in the absolute flux density scale. Because the quoted uncertainties reflect the scatter from determining flux densities in different ways, in some cases the relative uncertainties between the flux densities at 3 cm and 6 cm are smaller than the absolute uncertainty for either determination. The final flux densities and spectral indexes are listed in Tables 4 and 3. It is important to note that for resolved objects, the calculated spectral indexes may be lower limits (in the sense of objects appearing less optically thick than they truly are) depending on the geometry of the source; the observations are more sensitive to large-scale optically thin emission at 6 cm than at 3 cm, and the synthesized beams were  $\sim 1''.5$  at 3 cm and  $\sim 2''.0$  at 6 cm.

Table 1. New Observations

Target	RA (J2000)	Dec (J2000)	Date	Exp. Time	Config	Phase Calibrator(s)
0452-6927	4h 51m 53.00s	-69d 23' 29.99"	2002/5/6	169m	6A	0530-727
0452-6722	4h 52m 31.64s	-67d 17' 00.14"	2001/5/10-15	262m	6F	0355-669,0252-712,0407-658
0454-6716	4h 54m 49.92s	-67d 11' 58.80"	2001/5/11-15	249m	6F	0355-669,0252-712,0407-658
0456-6636	4h 56m 47.63s	-66d 32' 18.39"	2001/5/9	190m	6F	0515-674,0355-669
0457-6632	4h 57m 45.00s	-66d 27' 29.99"	2002/5/6	175m	6A	0530-727
0505-6807	5h 04m 59.76s	-68d 03' 40.03"	2001/5/9	190m	6F	0515-674,0355-669
0510-6857	5h 09m 50.00s	-68d 52' 59.99"	2002/5/6	166m	6A	0530-727
0519-6916	5h 18m 45.00s	-69d 14' 29.99"	2002/5/4	178m	6A	0530-727
0523-6806	5h 22m 55.00s	-68d 04' 29.99"	2002/5/4	174m	6A	0530-727
0525-6831	5h 24m 41.80s	-68d 29' 23.23"	2001/5/10	184m	6F	0515-674,0355-669
0531-7106	5h 31m 20.00s	-71d 04' 29.99"	2002/5/3	193m	6A	0530-727
0532-6629	5h 32m 35.00s	-66d 27' 19.99"	2002/5/4	174m	6A	0530-727
0538-7042	5h 38m 22.01s	-70d 41' 08.34"	2001/5/11-17	238m	6F	0530-727
0539-6931	5h 39m 11.36s	-69d 30' 04.51"	2001/5/11	186m	6F	0530-727
0540-6940	5h 39m 45.00s	-69d 38' 39.99"	2002/5/3	164m	6A	0530-727
0542-7121	5h 41m 30.00s	-71d 18' 59.99"	2002/5/3	164m	6A	0530-727
0545-6947	5h 45m 24.57s	-69d 46' 33.73"	2001/5/11	192m	6F	0530-727
0043-7321	0h 45m 29.90s	-73d 04' 56.63"	2001/5/14	220m	6F	0230-790
0046-7333	0h 48m 01.85s	-73d 16' 02.86"	2001/5/14	201m	6F	0230-790
0047-7343	0h 49m 31.70s	-73d 26' 50.26"	2001/5/14	200m	6F	0230-790
0057-7226	0h 59m 50.00s	-72d 10' 59.99"	2002/5/5	169m	6A	0230-790
0103-7216	1h 05m 16.67s	-72d 00' 04.64"	2001/5/10	212m	6F	0355-669,0252-712
0107-7327	1h 09m 12.00s	-73d 11' 41.99"	2002/5/6	159m	6A	0230-790
0122-7324	1h 24m 10.00s	-73d 08' 59.99"	2002/5/5	169m	6A	0230-790

Note. — MC targets are above the solid line, SMC below. “Target” refers to the Filipovic Parkes catalog name.

Table 2. Archival Observations

Target	RA (J2000)	Dec (J2000)	Date	Exp. Time	Config	Phase Calibrator	Program	Name
0452-6927	4h 51m 48.00s	-69d 23' 48.00"	2000/4/8	47m	6D	0454-810	C868	N79A
0452-6700	4h 52m 06.00s	-66d 55' 24.00"	2000/4/9	47m	6D	0454-810	C868	N4A
0454-6916	4h 54m 24.00s	-69d 10' 60.00"	2000/4/9	47m	6D	0454-810	C868	N83B-1
0456-6629	4h 57m 18.00s	-66d 23' 16.00"	2000/4/9	59m	6D	0454-810	C868	N11A
0540-6940	5h 39m 42.00s	-69d 38' 54.00"	2000/4/9	47m	6D	0454-810	C868	N160A
0540-6946	5h 40m 00.00s	-69d 44' 36.00"	2000/4/9	47m	6D	0454-810	C868	N159-5
0540-6946	5h 39m 39.50s	-69d 44' 26.00"	1996/7/11	75m	6C	0515-674	C520	lmcx1
0540-6946	5h 39m 38.72s	-69d 44' 45.97"	1995/8/30	70m	6D	0522-611	C462	0540-697
0043-7321	0h 45m 30.00s	-73d 04' 48.00"	2000/4/8	50m	6D	2353-686	C868	N12
0107-7327	1h 09m 12.00s	-73d 11' 42.00"	2000/4/8	47m	6D	2353-686	C868	N81
0122-7324	1h 24m 06.00s	-73d 08' 59.99"	2000/4/8	52m	6D	2353-686	C868	N88A

Note. — MC targets are above the solid line, SMC below. “Target” refers to the Filipovic Parkes catalog name, as for our observations, while “Name” refers to what the source was called by the archival observer.

High-resolution (6 km configuration) archival data were available for a few additional fields, and the sources detected in these data are included in Tables 4 and 3, identified with their ATNF program number. In some cases, the archival data were centered a few arcminutes (a significant fraction of the primary beam) away from our pointing, so the same sources are detected, but the errors are significantly lower in the pointing for which the source in question is nearer the center of the primary beam. The quality of the archival data vary, and in some cases is inferior to our data due to an insufficient frequency of observing the secondary phase calibrator during periods of varying atmospheric conditions. The data reduction and error assessment was performed identically to our data; cases in which the calibration was suspect are omitted, and cases in which we feel less accurate calibration was obtained are reflected by larger error bars.

### 3. The Population of Detected Sources

Many of the compact H II regions detected in this survey are associated with optically identified H II regions. This fact is not surprising as the H II regions observed in the radio are probably compact sites of embedded star formation associated with the less extinguished (and possibly more evolved) regions ionized by young stars and observable in optical light. Some of our radio sources have particularly interesting morphology, especially as compared to their infrared or H $\alpha$  emission, and we highlight these in detail in the appendix (A).

Tables 4 and 3 list all the detected compact radio continuum sources. Sources are named according to the nearest radio continuum source in the (low-resolution) Parkes surveys (Filipović, Haynes, White, & Jones 1998). If there is more than one compact source in the area, the compact source most clearly associated with the H II region as seen in the mid-IR is given the main designation, and other sources are designated with direction relative to the first one (e.g. “N”). Also listed are the nearest associated IRAS source, and the familiar shortened form (e.g. N23A for LHA 120-N 23A) of the Lamont-Hussey optical designation (Henize 1956). It is important to note, as mentioned above, that because the synthesized beam is smaller at 3 cm than at 6 cm, the spectral index is probably a lower limit that depends on the geometry of the source.

Table 3. Flux densities and spectral indexes of compact objects observed in the SMC.

radio source <sup>a</sup>	IRAS source <sup>b</sup>	RA <sup>c</sup> (J2000)	Dec (J2000)	F <sub>3</sub> <sup>d</sup>	F <sub>6</sub>	α <sup>e</sup>	log(Q) <sup>f</sup>	Sp.T. <sup>g</sup>	pgm <sup>h</sup>	notes, other IDs
B0043-7321	00436-7321	0 45 15.7	-73 6 7	< 3	0.8± .3		47.4	B0V		
B0043-7321(N)	00436-7321	0 46 13.1	-73 0 45	2 ± 1	0.6± .4	+1.5	47.8	O9.5V	C868	
				<15	1.1± .5		47.5	B0V		N12B?
				<10	1.6± .7		47.7	B0V	C868	
B0046-7333	00462-7331	0 48 8.5	-73 14 55	17 ± .5	17.4± .3	-0.0	48.8	O7.5V		N26
B0047-7343	00477-7343	0 49 29.0	-73 26 33	7.9± .4	8.4± .3	-0.1	48.4	O8.5V		N33
B0047-7343(N)	00469-7341	0 48 53.4	-73 24 57	1.2± 1.2	1 ± .3	+0.3	47.5	B0V		N33?
B0057-7226	00574-7226	0 59 14.9	-72 11 3	7 ± 2	2 ± 2	+1.8	48.4	O8.5V		N66, em* Lin 350
B0057-7226(S)	00574-7226	0 59 11	-72 11 40	5 ± 5	7 ± 7	-0.5	48.2	O9V		diffuse, N66
B0103-7216	01035-7215	1 5 4.1	-71 59 25	14.1± .4	14.1± .4	+0.0	48.7	B0V		N78B
B0103-7216(N)	01035-7215	1 5 5.2	-71 59 1	2.4± 1	2 ± 1	+0.3	47.9	O9.5V		N78A
B0107-7327	01077-7327	1 9 12.9	-71 11 39	34 ± 1	33 ± 1	+0.0	49.1	O6.5V		N81
B0107-7327(N)	01077-7327	1 9 20.6	-73 10 51	1.0± .6	1.5± .5	-0.6	47.5	B0V		N81
B0107-7327(W)	01077-7327	1 8 32.4	-72 11 19	.6± .4	.8± .3	-0.4	47.3	B0V		N81?
B0122-7324	01228-7324	1 24 7.9	-73 9 4	85 ± 1	91 ± .5	-0.1	49.5	O5V		N88
				87 ± 5	90 ± 4	-0.0	49.5	O5V	C868	

Note. — <sup>a</sup>Radio designation is from the Parkes survey of Filipović, Haynes, White, & Jones (1998). <sup>b</sup>IRAS source which was used to identify each object as a candidate UCH II region is also identified by name, and names are given for those objects which could be identified with optical HII regions. <sup>c</sup>Coordinates are J2000. <sup>d</sup>Flux densities are given in mJy. <sup>e</sup>α is the spectral index assuming  $F_\nu \propto \nu^\alpha$ . <sup>f</sup> $Q_{49}$  is the Lyman continuum flux assuming that all 3 cm emission is from an ionization-bounded optically thin HII region. For sources with no 3 cm detection,  $Q$  is calculated from the 6 cm flux density. Assumed distance to the SMC is 60 Mpc (Graczyk 2003, and references therein). <sup>g</sup>The spectral type of a single star required to produce the given  $Q$ . <sup>h</sup>The ATCA program number is given for archival data taken by other investigators.



Table 4. Flux densities and spectral indexes of compact objects observed in the LMC.

radio source	IRAS source	RA (J2000)	Dec (J2000)	F <sub>3</sub>	F <sub>6</sub>	$\alpha$	log(Q)	Sp.T.	pgm	notes, other IDs
B0452-6927	04521-6928	4 51 53.3	-69 23 29	160 ± 5	138 ± 3	+0.2	49.6	O5V		N79A
				169 ± 5	133 ± 5	+0.3	49.6	O5V	C868	
B0452-6927(E)	04521-6928	4 51 53	-69 23 27	30	25	+0.3	48.8	O7.5V		4 weak sources on E edge of main source
B0452-6700(SW)	04520-6700	4 52 9	-66 55 23	45 ±15	27 ±10	+0.7	48.7	O8V	C868	elongated, N4A
B0452-6700(NE)	04520-6700	4 52 12	-66 55 15	5 ±10	8 ± 8	-0.7	48.1	O9V	C868	N4A
B0452-6722(NW)	04524-6721	4 52 12.4	-67 12 52	3.5± 2	2.3± .3	+0.6	47.9	O9.5V		N5?
B0452-6722(NE)	04524-6721	4 52 33.4	-67 13 28	2.4± .5	0.9± .3	+1.4	47.7	B0V		N5?
B0454-6916(E)	04546-6915	4 54 26.1	-66 11 2	39.3± 2	39.1± 1	+0.0	49.0	O6.5V	C868	N83B
B0454-6916(W)	04542-6916	4 53 58.6	-66 11 6	2.8± 1	3.6± .5	+0.4	47.8	O9.5V	C868	N83B
B0456-6629(E)	04571-6627	4 57 16.2	-66 23 21	30 ± 5	31 ± 5	+0.0	48.8	O7.5V		diffuse, N11A
				32 ± 5	32 ± 5	+0.0	48.9	O7V	C868	
B0456-6629(W1)	04566-6629	4 56 57.3	-66 25 13	<10	3.3± .4		47.9	O9.5V		N11B
				1.5± .8	3.1± 1.7	-1.0	47.5	B0V	C868	
B0456-6629(W2)	04566-6629	4 56 47.8	-66 24 34	—	9 ± 2		48.3	O9V		diffuse, N11B
				1.2± 1.5	7 ± 5	-2.5	48.1	O9V	C868	
B0457-6632	04576-6633	4 57 41.0	-66 30 36	2 ± .6	2.6± .3	-0.4	47.7	B0V		diffuse
B0505-6807	05051-6807	5 5 5.7	-68 3 46	1.0± .4	1.2± .2	-0.3	47.4	BOV		N23A
B0505-6807(N)	05051-6807	5 5 9.7	-68 1 37	1.6± .6	1.1± .3	+0.5	47.6	BOV		N23A
B0510-6857(W)	05101-6855A	5 9 50.6	-68 53 5	39 ± 1	26 ± 1	+0.6	49.0	O6.5V		N105
B0510-6857(E)	05101-6855A	5 9 52.9	-68 53 0	30 ± 4	31 ± 2	-0.0	48.8	O7.5V		N105
B0510-6857(N)	05101-6855A	5 9 52.5	-68 52 47	9 ± 7	9.5± 1.5	-0.1	48.3	O9V		diffuse, N105
B0510-6857(S)	05101-6855A	5 9 52.1	-68 53 25	12 ± 7	14 ± 2	-0.2	48.4	O8.5V		diffuse, N105
B0519-6916(E)	05196-6915	5 19 39.3	-69 13 43	5 ± 5	2.1± .4	+1.2	47.6	B0V		N119?
B0519-6916(N1)	05195-6911	5 18 55.4	-69 9 0	7 ± 7	4 ± .5	+0.8	47.9	O9.5V		N119?
B0519-6916(N2)	05195-6911	5 18 50.0	-69 9 32	6 ± 7	5.5± .5	+0.1	48.1	O9.5V		N119?
B0523-6806(NE)	05233-6802	5 23 43.5	-68 0 34	10 ±10	10 ± .5	-0.0	48.3	O9V		N44M
B0522-5800	05221-6800 +05223-6801	5 22 12.6	-67 58 32	—	34 ± 1.5		48.9	O7V		N44B,C
B0523-6806(SE)	05230-6807	5 23 24.7	-68 6 41	4.5± 2	4.8± 2	-0.1	48.0	O9.5V		N44?
B0523-6806(SW)	05224-6807	5 22 19.6	-68 4 37	11 ± 1.5	10 ± 1	+0.1	48.4	O8.5V		N44G,K
B0523-6806	05230-6807	5 22 55.2	-68 4 9	3 ± .3	3.3± .3	-0.1	47.8	B0V		compact source only, N44D
B0525-6831	05253-6830	5 25 6	-68 28 15	10 ± 5	10 ± 5	+0.0	48.4	O8.5V		diffuse, N138A
B0525-6831(N)	05253-6830	5 24 50.5	-68 26 55	< .5	.8± .3		47.2	B0.5V		N138?
B0525-6831(W)	05244-6832	5 24 10.5	-68 30 26	< 1.5	.4± .3		46.9	B0.5V		N138B,D
B0531-7106	05320-7106	5 31 22.9	-71 4 9	2.1± .5	2.1± .3	+0.0	47.7	B0V		compact core only, N206A

Table 4—Continued

radio source	IRAS source	RA (J2000)	Dec (J2000)	F <sub>3</sub>	F <sub>6</sub>	$\alpha$	log(Q)	Sp.T.	pgm	notes, other IDs
B0531-7106(SW1)	05313-7109	5 30 56.3	-71 6 2	6 ± 3	6 ± 3	+0.0	48.1	O9V		diffuse, N206
B0531-7106(SW2)	05310-7110	5 30 20.6	-71 7 44	20 ±20	11 ± 7	+0.9	48.4	O8.5V		diffuse, N206B
B0531-7106(SW3)	05310-7110	5 30 31.3	-71 8 56	4 ± 5	2.7± .6	+0.6	47.8	O9.5V		N206B
B0531-7106(SE)	05310-7106	5 32 18.6	-71 7 44	9 ±10	1.7± .8	+2.4	47.6	B0V		N206?
B0532-6629	05325-6629	5 32 32	-66 27 15	1 ± .2	.8± .1	+0.3	47.4	B0V		compact, N55A
B0532-6629(NE)	05325-6629	5 32 33	-66 27 8	5 ± .8	4 ± .5	+0.3	48.1	O9.5V		diffuse, N55A
B0538-7042(S)	05389-7042	5 38 24.2	-70 44 26	4.5± .5	5.5± .6	-0.3	48.0	O9.5V		N213?
B0538-7042(E)	05389-7042	5 38 26.9	-70 41 6	1.0± .3	1.1± .3	-0.1	47.4	B0V		N213
B0538-7042	05389-7042	5 38 21.5	-70 41 5	42 ± 2	26 ± 2	+0.7	49.0	O6.5V		N213, diffuse
B0539-6931(1)	05396-6931	5 39 15.7	-69 30 39	12 ± 2	15.5± 2	-0.3	48.4	O8.5V		N158C
B0539-6931(2)	05396-6931	5 39 17.4	-69 30 49	3.5± 2	3.3± 1	+0.1	47.9	O9.5V		N158C
B0539-6931(N)	05391-6926	5 38 44.5	-69 24 38	20 ±20	5.2± 2	+2.0	48.1	O9V		N158?
B0540-6935	05404-6933	5 39 40.0	-69 32 56	<10	2.7± 1		47.8	O9.5V		N158?
B0540-6940(1)	05401-6940	5 39 46.0	-69 38 39	120 ± 7	130 ± 7	-0.1	49.4	O5V		N160A2
				111 ±10	127 ± 9	-0.2	49.4	O5V	C868	
B0540-6940(2)	05401-6940	5 39 44.3	-69 38 48	16 ± 1	16 ± 1	+0.0	48.6	O8V		N160A3?
				12 ± 5	15 ± 5	-0.3	48.4	O8.5V	C868	
B0540-6940(3)	05401-6940	5 39 43.4	-69 38 54	50 ± 5	50 ± 5	+0.0	49.1	O6.5V		N160A1
				52 ±10	47 ±10	+0.1	49.1	O6.5V	C868	
B0540-6940(4)	05401-6940	5 39 39.0	-69 39 11	12 ± 1	14.5± 1	-0.2	48.4	O8.5V		N160A, maser
				16 ± 5	11 ± 5	+0.5	48.6	O8V	C868	
B0540-6940(5)	05401-6940	5 39 38.8	-69 39 04	8.0± 1	6.0± 1	+0.4	48.3	O9V		N160A
				<10	6 ±10		48.1	O9V	C868	
B0540-6940(E)	05409-6942	5 40 25.2	-69 40 14	—	15 ± 6		48.5	O8V		N160C
B0540-6946(1) <sup>a</sup>	05405-6946	5 40 4.4	-69 44 37	50 ±75	70 ±15	-0.5	49.2	O6V		N159D
				43 ±15	64 ± 8	-0.6	49.0	O6.5V	C868	3 cm calibration suspicious
				60 ±55	55 ±10	+0.1	49.1	O6.5V	C520	
				68 ±20	70 ± 7	-0.0	49.2	O6V	C462	
B0540-6946(4)	05401-6947	5 39 37.5	-69 45 26	—	120 ±15		49.4	O5.5V		N159A
				110 ±15	123 ± 8	-0.2	49.4	O5.5V	C520	
				97 ±10	122 ± 8	-0.3	49.4	O5.5V	C868	
B0540-6946(5)	05401-6947	5 39 37.5	-69 46 10	—	30 ± 5		48.8	O7.5V		N159A
				35 ±20	32 ±10	+0.1	48.9	O7V	C520	
B0542-7121	05423-7120	5 41 37.5	-71 19 02	19 ± 2	18 ± 1.5	+0.1	48.6	O8V		S169, N214C, knots w/halo

Table 4—Continued

radio source	IRAS source	RA (J2000)	Dec (J2000)	F <sub>3</sub>	F <sub>6</sub>	$\alpha$	log( $Q$ )	Sp.T.	pgm	notes, other IDs
B0542-7121(N)	05423-7120	5 41 17.8	-71 16 39	1.8± .6	.9± .3	+1.0	47.6	B0V		N214H
B0545-6947(N)	05458-6947	5 45 4.3	-69 39 28	—	7.3±1		48.2	O9.5V		
B0545-6947(NE)	05458-6947	5 45 57.3	-69 43 56	1.3± 1.5	2.1± .5	-0.7	47.7	B0V		N168?
B0545-6947(1)	05458-6947	5 45 27.8	-69 46 23	12.3± 1.5	13.1±1.5	-0.1	48.5	O8V		N168A
B0545-6947(2)	05458-6947	5 45 20.0	-69 46 45	2.7± .5	2.7± .5	+0.0	47.8	O9.5V		N168B

<sup>a</sup>numbering scheme follows Hunt & Whiteoak (1994).

Note. — All units and columns as Table 3. Adopted distance to the LMC is 50 kpc (Alcock et al. 2003).

The properties of the population of detected compact H II regions should be sensitive to the physics of star formation in the Magellanic Clouds. As our sample was selected to probe the most compact and densest H II regions, we probe both the individual star formation mechanism and the formation mechanism of clusters, if indeed these are different. In the following sections we first compare the IRAS and radio properties of the sample. We also model the total luminosity and Lyman-continuum flux distributions, which are sensitive to the stellar and cluster initial mass functions. Finally we look for any trends involving the radio spectral index. Analysis of the high-resolution IR properties of the sample will be presented in a future paper.

### 3.1. Spectral Indexes and FIR Colors

One can describe a source’s spectral shape near  $\lambda=3\text{--}6$  cm with a single number  $\alpha$  if one assumes that the flux density is a power-law function of frequency  $F_\nu \propto \nu^\alpha$ . Optically thin and optically thick thermal radiation have spectral indexes of  $\alpha=-0.1$  and  $\alpha=2$  (blackbody limit), respectively. Figure 2 shows the spectral indexes of detected sources, showing many that are consistent with thermal radiation, as well as some which are probably background nonthermal sources. The spectral index of the compact sources detected is often larger (more consistent with thermal radiation or a higher optical depth) than the spectral index calculated for the same source from the relatively low resolution Parkes data. This is expected physically, because the more diffuse emission around a compact embedded source will be optically thin, driving the spectral index from a positive value toward zero.

We used the WC89 FIR color criteria to select our sources, in order to maximize the chances of finding compact thermal sources, or ultracompact H II regions. While the selection criterion did yield a very high detection rate of compact sources, many of which have flat or inverted (optically thick thermal) spectral indexes, there do not appear to be any clear correlations between the FIR color and the optical depth of associated compact sources. Figure 3 explores various possible correlations between FIR (low-resolution) color and flux density, and high-resolution cm spectral index and flux density. Nonthermal sources are plotted with thin lines and excluded from analysis of correlations. There is a weak trend for sources with higher  $12\mu\text{m}$  flux densities to have higher 3 cm flux densities in compact sources. The Pearson correlation coefficient is 0.51 and the slope between  $\log(F_{12\mu\text{m}})$  and  $\log(F_{3\text{cm}})$  is  $0.50\pm 0.17$ . Including nonthermal sources decreases the correlation coefficient to 0.41, and the slope to  $0.40\pm 0.16$ . There is also a weak trend for brighter  $12\mu\text{m}$  IRAS sources to have an envelope of redder 24/12 $\mu\text{m}$  colors. The Pearson correlation coefficient between IRAS color and IRAS  $12\mu\text{m}$  flux density is only 0.14, consistent with an envelope effect.

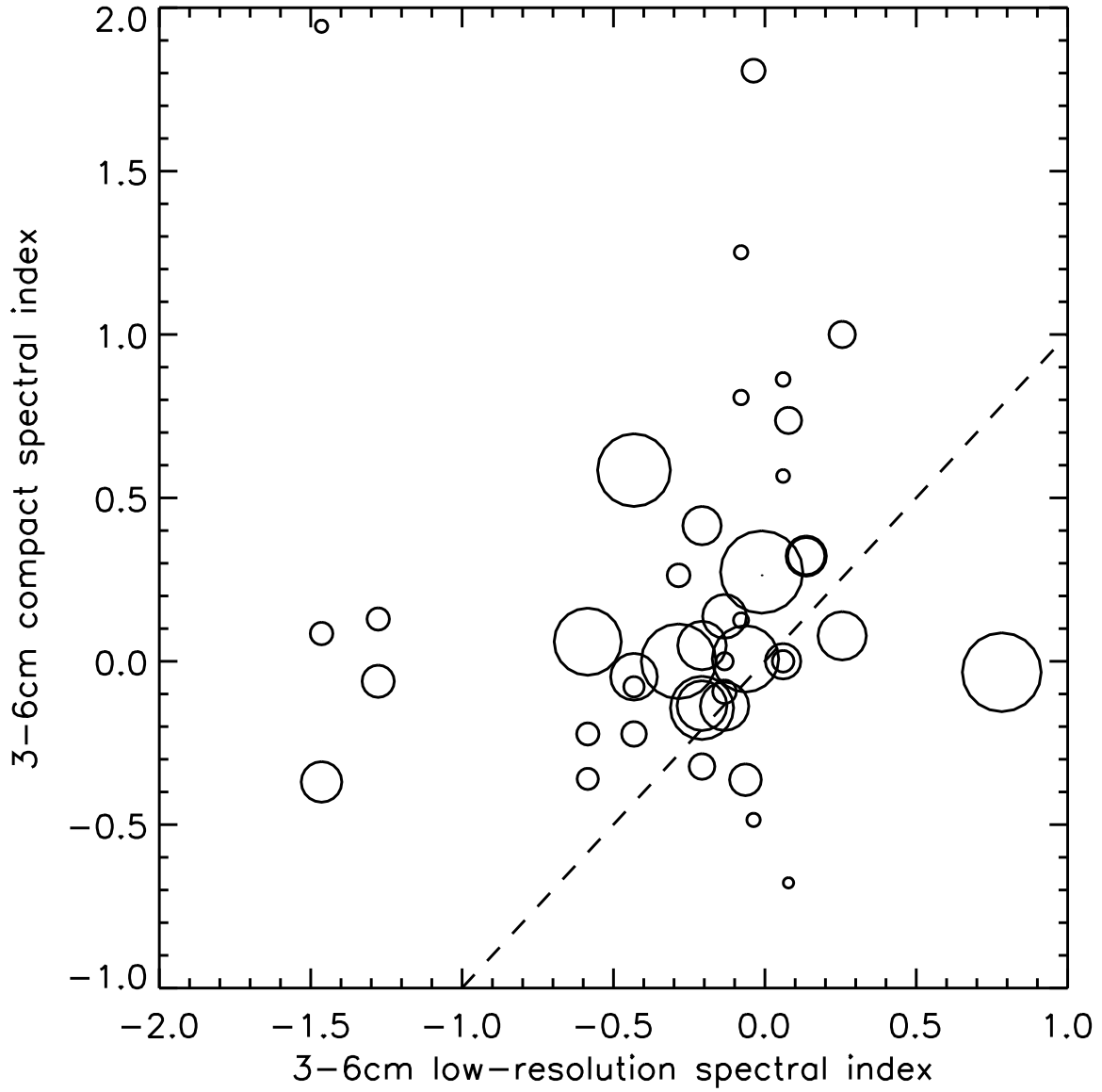


Fig. 2.— 3-6 cm spectral indexes of detected sources, assuming that the flux density is a power-law function of frequency  $F_\nu \propto \nu^\alpha$ . The size of the data point scales with the signal-to-noise of the detected source. The spectral indexes tend to be more positive (more optically thick thermal) at higher resolution.

Our sample could address whether there is any correlation between the luminosity of an H II region and how embedded it is (as indicated by the radio spectral index). It has been suggested (e.g. Beckman et al. 2000) that there is a change from ionization-bounded to density-bounded as the luminosity of an H II region increases. These investigators also find that more H $\alpha$ -luminous H II regions leak more ionizing radiation than less H $\alpha$ -luminous ones. The lower left panel of Figure 3 shows the spectral index of our H II regions as a function of 3 cm flux density. There is no discernible trend – H II regions powered by more numerous or more massive ionizing stars show the same range in H II region density as less luminous regions. There is also no correlation between IRAS color and radio spectral index – a redder IRAS color does not predict a more optically thick compact H II region. The correlation coefficients for radio spectral index with radio flux density and IRAS color are -0.02 and -0.16, respectively.

### 3.2. Modeled Size and Density

We can model the radio spectral energy distribution of each source as a compact spherical H II region of constant density and electron temperature. These simple models allow for only two free parameters, radius and electron density. It is assumed that the radio emission is purely thermal in nature, but the free-free emission may be self-absorbed in order to reproduce spectral indices of  $\alpha > -0.1$  (sufficiently large electron densities cause the radio spectral energy distribution to become “inverted” due to self-absorption at lower frequencies). The radio emission is calculated for each chord through the sphere parallel to the line of sight, and this is integrated over the projected circle perpendicular to the line of sight (simple radiative transfer without scattering). More complex models are possible, but not warranted since we only have two data points for each region. Figure 4 shows the modeled radii and densities of the sources that are consistent with thermal emission. The spectral shape of thermal emission at frequencies above that at which the emitting source is optically thin is fairly insensitive to the source density. Therefore we only model source densities above  $10^3 \text{ cm}^{-3}$ . For sources consistent with lower densities, we give the radius of a  $10^3 \text{ cm}^{-3}$  source as a lower limit to the radius.

### 3.3. Exciting Star(s) Ionizing Flux

If one assumes that each thermal compact radio source is an H II region and that the radio continuum emission comes exclusively from optically thin thermal bremsstrahlung radiation, the number of ionizing photons required to ionize the source is derived by (Condon

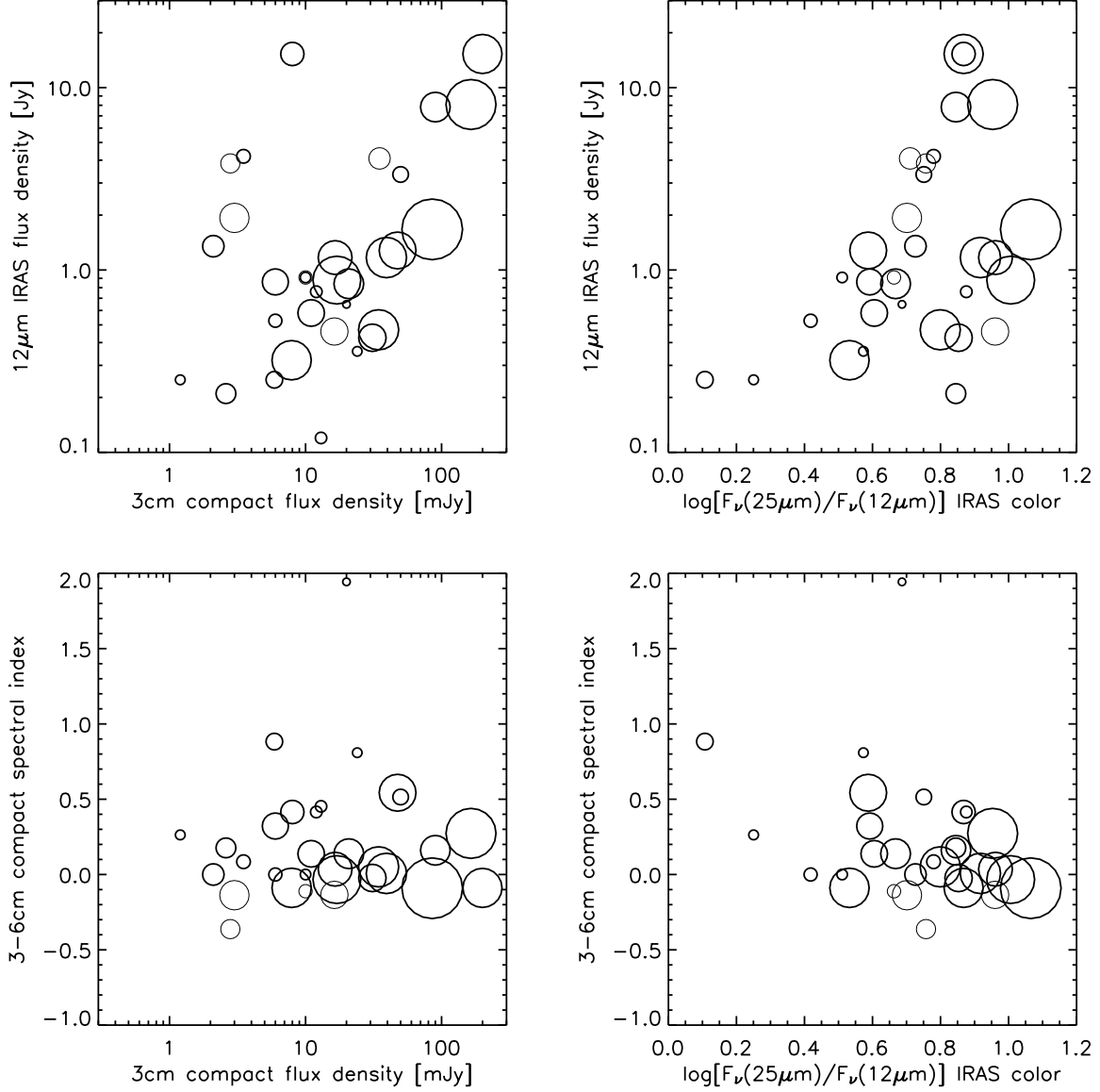


Fig. 3.— The various relationships between IRAS color, IRAS flux density, 3 cm compact source flux density, and 3/6 cm compact source spectral index are explored. The size of the data point scales with the signal-to-noise of the detected source. The flux densities of several compact radio sources are summed in cases where more than one compact source is associated with a single IRAS source. Nonthermal sources are plotted with a thin line and excluded from analysis of correlations (see text).





1992),

$$Q \geq 6.3 \times 10^{52} s^{-1} \left( \frac{T_e}{10^4 K} \right)^{-0.45} \left( \frac{\nu}{GHz} \right)^{0.1} \left( \frac{L_{thermal}}{10^{27} ergs^{-1} Hz^{-1}} \right),$$

where  $T_e$  is the electron temperature of the nebula,  $\nu$  the frequency of observation, and  $L_{thermal}$  the observed luminosity. The Lyman continuum flux  $Q$  calculated from the 3 cm flux density (or the 6 cm flux density for sources with no 3 cm detection) is included in Tables 3 and 4. Note that these values are lower limits due to the assumption that the emission is optically thin. The spectral type of a single star required to produce the given ionizing flux is also tabulated, using the conversions from Smith, Norris, & Crowther (2002) and Crowther (private communication, 2003).

As a self-consistency check on the ionizing flux calculated using the simple Condon (1992) formula and on the simple constant-density models, we calculate the number of ionizing photons required to ionize each modeled region, assuming photoionization equilibrium. Figure 5 shows that the  $Q$  values calculated using the two methods agrees favorably. The main source of the small discrepancies in the assumption of the emission being optically thin in the Condon relation above; if the emission is self-absorbed,  $L_{thermal}$  will be underestimated.

### 3.4. Cluster Luminosity Function

The luminosity function of extragalactic H II regions can be fit with a power law of index  $a=-2.0\pm 0.5$ , i.e.  $dN(L) \propto L^a dL$ . This result is similar for H $\alpha$  luminosities (e.g. Kennicutt, Edgar, & Hodge 1989), radio luminosities (e.g. McKee & Williams 1997, and references therein), and optical luminosities (e.g. Larsen 2002, in particular  $a=-2.01\pm 0.08$  for the LMC). Elmegreen & Efremov (1997) propose that this is due to a universal formation mechanism: all types of clusters form with constant efficiency in molecular clouds, so the cluster mass distribution reflects the interstellar cloud mass distribution, which has an index  $\sim -2$ .

The H II region or cluster luminosity function is related to the distribution of the number of cluster member stars  $N_*$  (or cluster mass), and to the stellar initial mass function (IMF). Oey & Clarke (1998) provide a detailed explanation of how these distributions are related. They draw attention to the particularly important effect of small-number statistics. In rich, luminous clusters with many stars, the stellar IMF is statistically populated out to a fairly high mass, and the cluster luminosity simply reflects the total cluster mass. The cluster luminosity function in this regime, which Oey & Clarke (1998) call “saturated” then simply reflects the cluster mass distribution, a power-law  $dN(M_c) \propto M_c^\beta dM_c$ , with index  $\beta=-2$ . Sparser clusters are dominated by one or a few high-mass members – the statistical

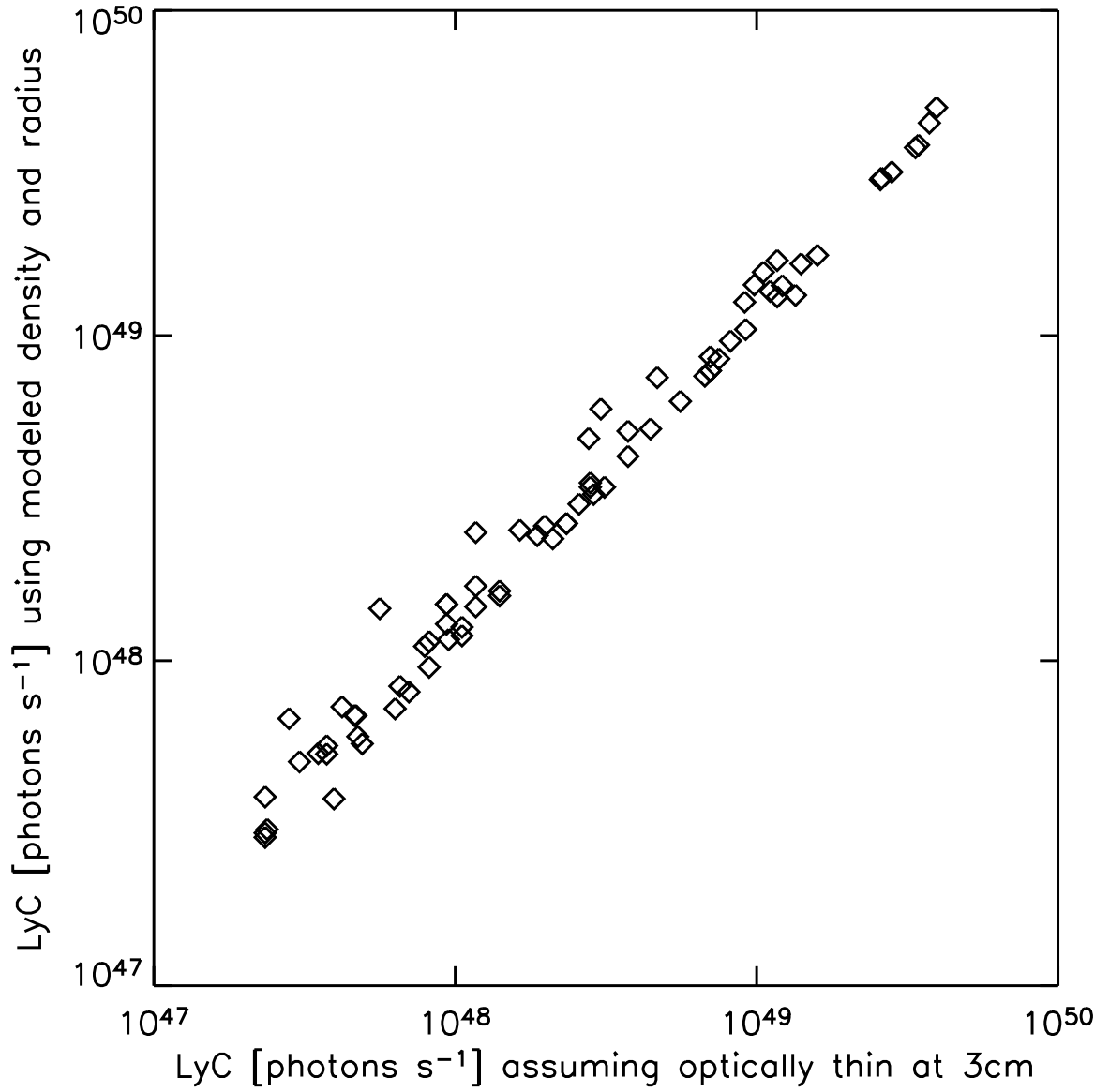


Fig. 5.— Lyman continuum fluxes calculated from the Condon (1992) formula and the 3 cm flux density, and calculated from the density and radius modeled to fit both flux densities. The methods agree well, with the model flux sometimes larger than the 3 cm-derived flux, probably for sources that are not completely optically thin at 3 cm.

variation in luminosity of clusters of a given mass can become large due to poor sampling of the stellar IMF. This flattens the cluster luminosity function at the faint end, and in fact can transform power-law behavior into a more rounded distribution (see e.g. Fig. 4 in Oey & Clarke 1998).

Figure 6 shows the luminosity distributions of all IRAS sources satisfying the WC89 color criteria, and all of our selected candidate UCH II sources. The bolometric luminosity has been estimated for each H II region by the sum over the 4 IRAS bands of  $\sum_{i=1}^4 \nu(i) F_{\nu(i)}$  (e.g. Casassus, Bronfman, May, & Nyman 2000). The distributions flatten, probably due to the statistical effect described above. Single massive stars have luminosities of  $\sim 10^5 L_{\odot}$ , so most of our sample is probably in the regime of “unsaturated” stellar IMF statistics. The turnover of the luminosity function at the faint end ( $L \lesssim 10^5 L_{\odot}$ ) is due to confusion-induced incompleteness resulting from the quite large IRAS beam (e.g.  $\sim 50$  pc at  $60 \mu\text{m}$  at the distance of the Magellanic Clouds). The confusion limit for sources (Condon 1974) with a uniform spatial distribution and following a power law luminosity distribution with is about 10 beams/source. The effective resolution of the IRAS point source catalog is a nontrivial function of the spatial distribution of emission, but the expected confusion limited source densities are about 40, 40, 15, and 5 sources  $\text{deg}^{-2}$  at 12, 25, 60, and 100  $\mu\text{m}$ , respectively (compare to the source densities at which special “high density” algorithms were invoked in constructing the IRAS catalog: 45, 45, 16, and 6 sources  $\text{deg}^{-2}$ ). This translates into confusion limited flux densities of 0.3, 0.3, 2, and 20 Jy at 12, 25, 60, and 100  $\mu\text{m}$  (verified by inspection of the point source catalog in the LMC), and an estimated confusion limited total luminosity in the Clouds of  $2.5 \times 10^{38}$  erg/s ( $7 \times 10^4 L_{\odot}$ ). The luminosity function of all IRAS sources with H II region colors (solid curve in Fig. 6) indeed turns over about that confusion limited luminosity.

It is reassuring to note that the distributions above their peaks have the same power-law indexes within errors ( $-1.67 \pm 0.3$  for the full color-selected sample and  $-1.60 \pm 0.5$  for our “radio-aware” selection), and despite a slight bias toward observing brighter sources, we have not apparently affected our sample with selection effects beyond those unavoidable results of low spatial resolution previous observations.

It is possible to quantify the constraints that our sample, selected to probe the most compact and densest H II regions, places on the stellar and cluster mass functions. We use Monte-Carlo methods to model the cluster luminosity function, similar to the process followed by Oey & Clarke (1998) and Casassus, Bronfman, May, & Nyman (2000). We assume that the cluster masses  $M_c$  follow a power-law distribution

$$p(M_c) \propto M_c^{-\beta}$$

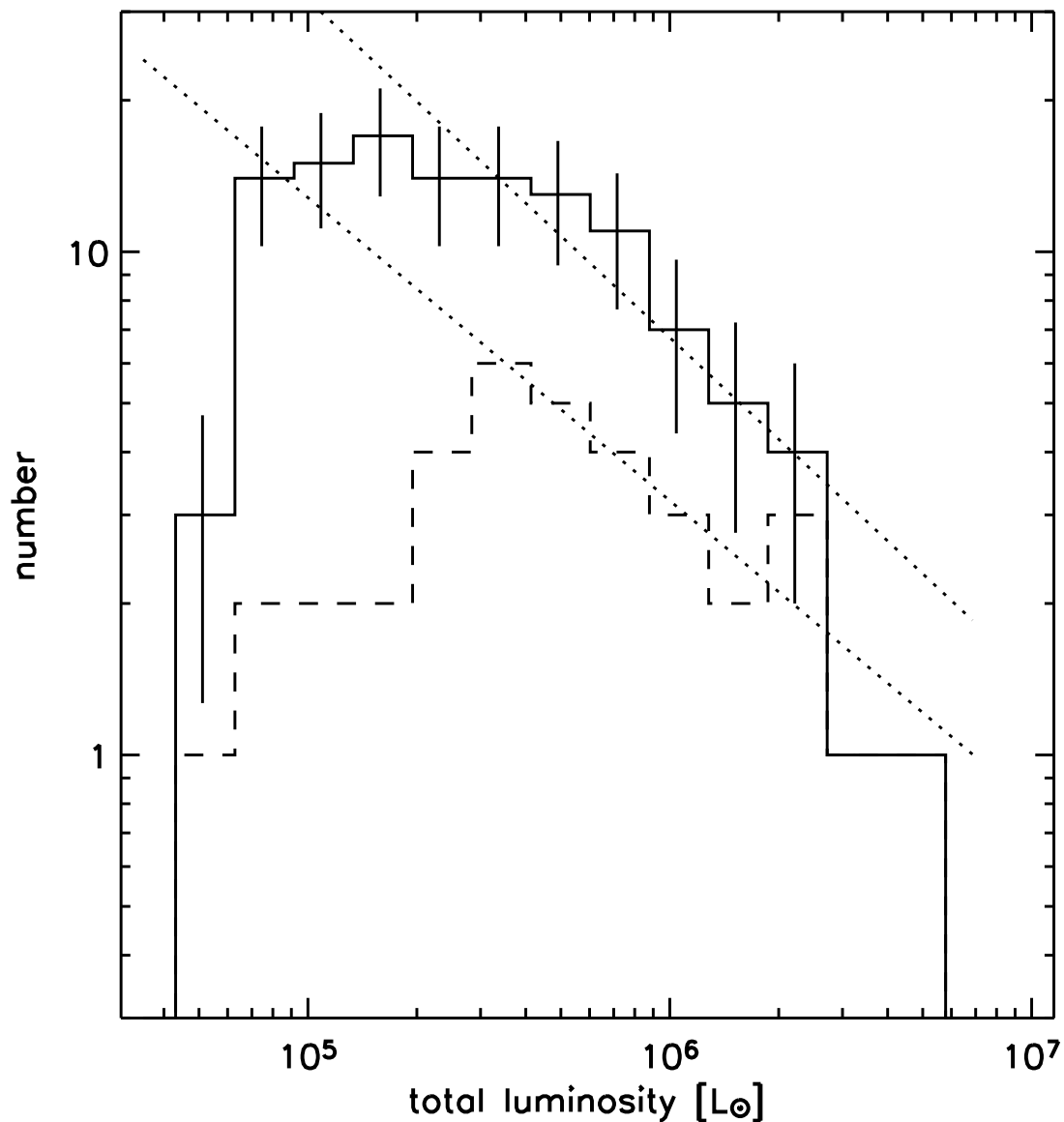


Fig. 6.— Total luminosity function of all IRAS sources in the Magellanic Clouds that satisfy the WC89 color criteria for UCH II regions (solid), and of our candidate sources (selection criteria described in the text). Power laws are fitted to the unconfused bright end of the distribution, and have indices of  $-1.67 \pm 0.3$  and  $-1.60 \pm 0.5$  for the full and subselected populations ( $dN(L) \propto L^{-1.67} dL$ ).

and that the stars in the cluster follow a standard stellar initial mass function (IMF)

$$p(M_{\star}) \propto M_{\star}^{-(1+\gamma)}.$$

Casassus, Bronfman, May, & Nyman (2000) imposed a power-law on the number of stars per cluster

$$p(N_{\star}) \propto N_{\star}^{-\beta},$$

rather than on the cluster mass. We prefer to use the cluster mass because it has physical meaning and may be related to the interstellar cloud mass distribution. The synthetic luminosity functions constructed either way are quantitatively consistent. We assume that because we selected for young star-forming H II regions, that our cluster population can be adequately modeled as unevolved. Oey & Clarke (1998) showed that evolution can be an important effect for older H II regions (e.g. in interarm regions of spiral galaxies), as the most massive stars in the cluster die off, and the more numerous less massive stars become more important to ionizing the cluster.

Figure 7 shows the index of a power-law fit to the bright end of the cluster luminosity function as a function of IMF power-law index  $\gamma$  and of the cluster mass function power-law index  $\beta$ . The results are insensitive to the stellar and cluster mass upper and lower cutoffs (for this particular run  $(0.5,120) M_{\odot}$  and  $(4,12000) M_{\odot}$ , respectively). Such a fitted power-law is sensitive to the range over which one fits, since the luminosity function rolls over, so Figure 4 should be used to understand qualitative trends, with possible systematic offsets in the index (by 0.1–0.2) if a different luminosity range is used. The effects of poor statistics on the form of the luminosity function have been well-described by Oey & Clarke (1998): The high-L end of the distribution is defined by a chance collection of particularly massive stars and can fall off very quickly. At the faint end, the distribution is flattened by the spread in L for a given cluster mass. In this statistically unsaturated regime, the *cluster* luminosity function index is much more strongly dependent on the *stellar* mass function index than the cluster mass function index. Due to the steepness of the mass-luminosity relation for main-sequence stars, it is not hard to make a fairly bright cluster with a small number of massive stars. Instead of enforcing a power-law on either data or model, we fit the bright (unconfused) part of the observed luminosity function to theoretical models. The best fit is for  $\gamma=1.5\pm0.25$  and  $\beta=2.0\pm0.5$ .

It is even more interesting to fit the distribution of Lyman continuum photon fluxes  $Q$ .  $Q$  is determined here from our radio observations, so this constitutes analysis of our observations, rather than analysis of the input sample (the total luminosities were calculated from IRAS flux densities). The  $Q$  distribution of our observed compact radio sources is shown in Figure 8. The observed (and modeled)  $Q$  functions are even less easily understood as power laws; the  $Q$ -distribution is even further into the statistically unsaturated regime,

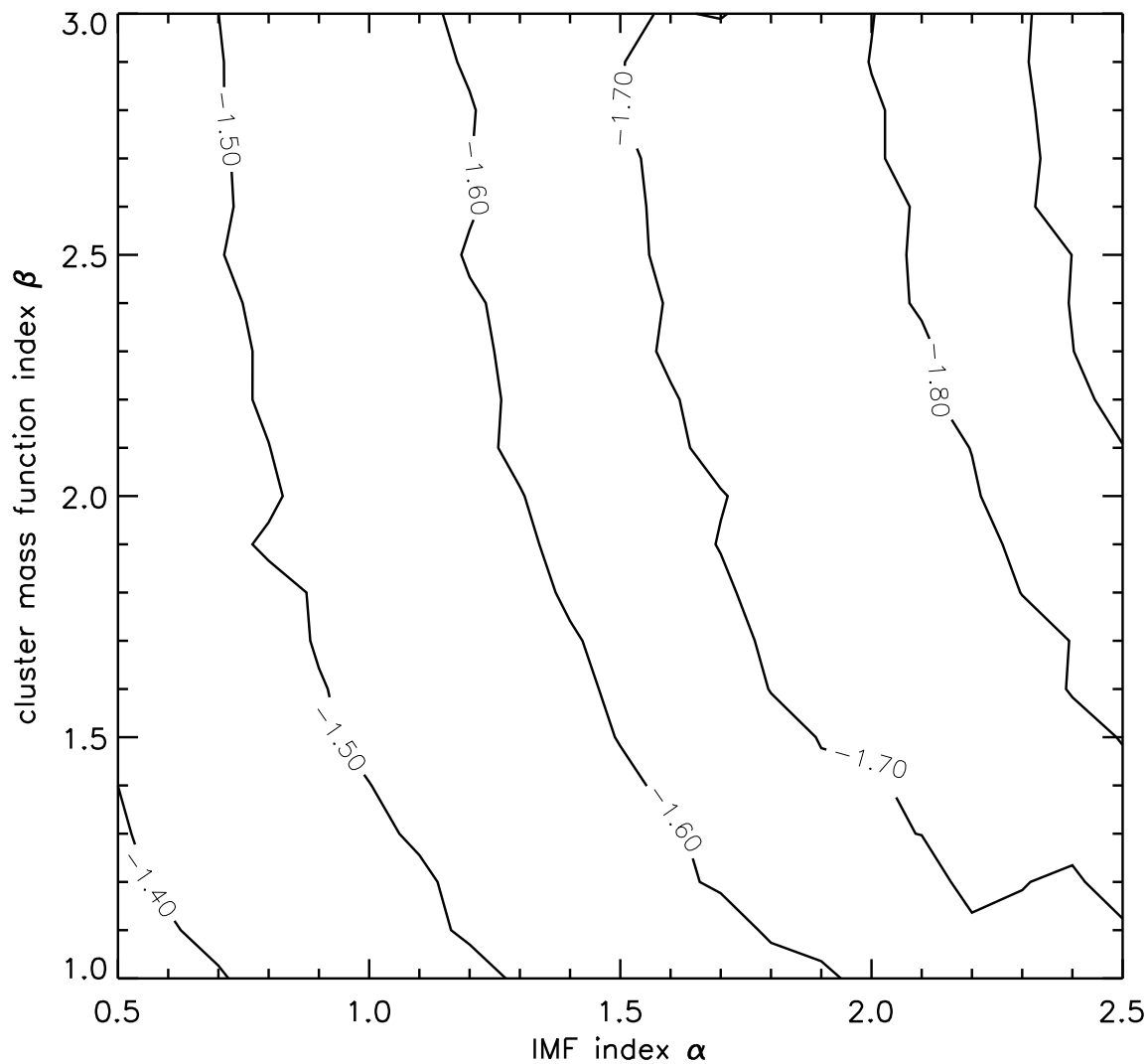


Fig. 7.— The index of a power-law fit to the bright end of a synthetic cluster luminosity function, as a function of stellar IMF index  $\gamma$  and cluster mass function index  $\beta$ . For this sample, the cluster luminosity function index is  $a \approx -1.65$ , which corresponds to a standard stellar initial mass function of  $\gamma \approx 1.5$ , but is fairly insensitive to the cluster mass function.

because of the extremely steep mass- $Q$  relation for main sequence stars (even steeper than the mass-luminosity relation). For illustration only, we proceed to fit a power-law to the portion of the distribution which is relatively straight, and show the index of this power-law as a function of  $\gamma$  and  $\beta$  in Figure 9. As with the total cluster luminosity, the  $Q$  distribution is more sensitive to the stellar IMF index  $\gamma$  than the cluster mass function index  $\beta$ . Again, we search for the model distribution which best fits the data without imposing a power-law, and find  $\gamma=1.4\pm0.2$  and  $\beta=2.1\pm0.3$ . These indexes agree with those determined from the total IRAS luminosity (at much lower resolution), and with observations and theories of star formation in the Milky Way.

#### 4. Conclusions

We conducted a radio continuum survey of UCH II candidates in the Magellanic Clouds using the highest resolution configuration of the Australia Telescope Compact Array. Candidates were selected from IRAS and lower resolution radio continuum measurements, using the far-IR colors determined by Wood & Churchwell (1989b) to be characteristic of UCH II regions. We find a very high success rate for detecting compact radio sources with spectral indexes consistent with thermal emission based on these selection criteria, even with the relatively poor spatial resolution of the IRAS survey. This detection rate is at least in part due to the thermal infrared luminosities of UCH II regions; UCH II regions are among the most luminous Galactic objects in the IRAS catalog ( $> 60\%$  of the IRAS sources with flux densities  $> 10^4$  Jy at  $100\mu\text{m}$  are UCH II regions Wood & Churchwell 1989a). Consequently, UCH II regions will tend to be dominant sources at thermal infrared wavelengths, making them relatively easy to detect based on their infrared colors despite contaminating sources within the resolution element. This is good news for inferences drawn from infrared observations with the *Spitzer* Space Telescope and ASTRO-E satellites, which probe similar spatial scales in nearby galaxies as IRAS did in the Magellanic Clouds.

In many of the cases where such information is available, we find that the compact radio sources are found in the densest, highest excitation parts of H II region complexes. Simple models of the radio sources as constant-density spheres have electron densities of a few times  $10^3$  to  $10^6$   $\text{cm}^{-3}$ , and sizes ranging from 0.01 to 0.1 parsecs, reasonable physical characteristics for compact and ultra-compact H II regions. We are clearly sampling the population of youngest embedded H II regions in the Clouds.

We compare the radio flux densities of our detected compact sources with the infrared flux densities of the candidate regions, and with radio flux densities at lower spatial resolution. Many of the radio sources have spectral indexes that are consistent with thermal

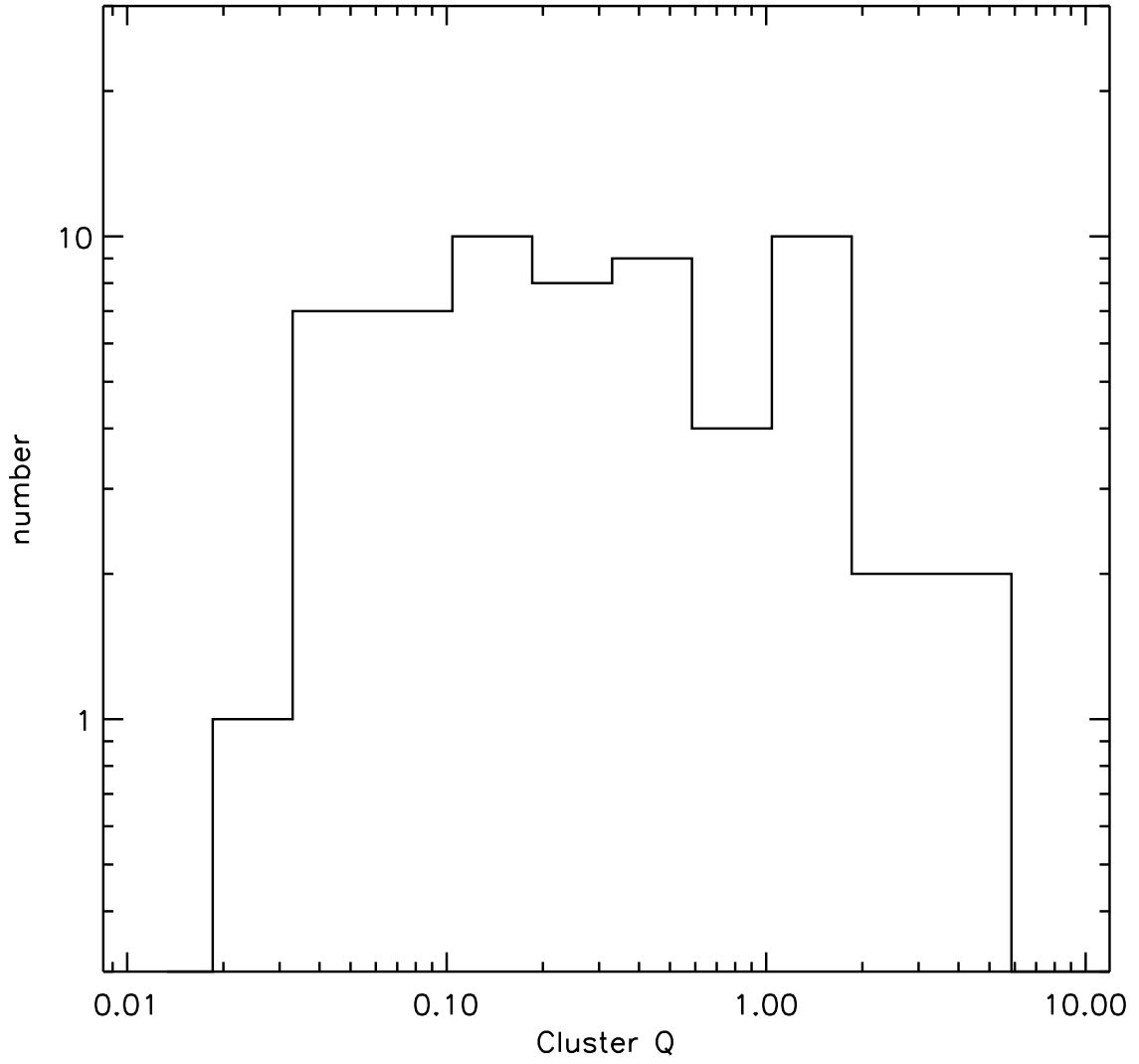


Fig. 8.— The distribution of Lyman continuum fluxes  $Q$  implied for the observed compact radio sources.  $Q$  is quoted in units of  $1 \times 10^{49}$  photons  $s^{-1}$ .



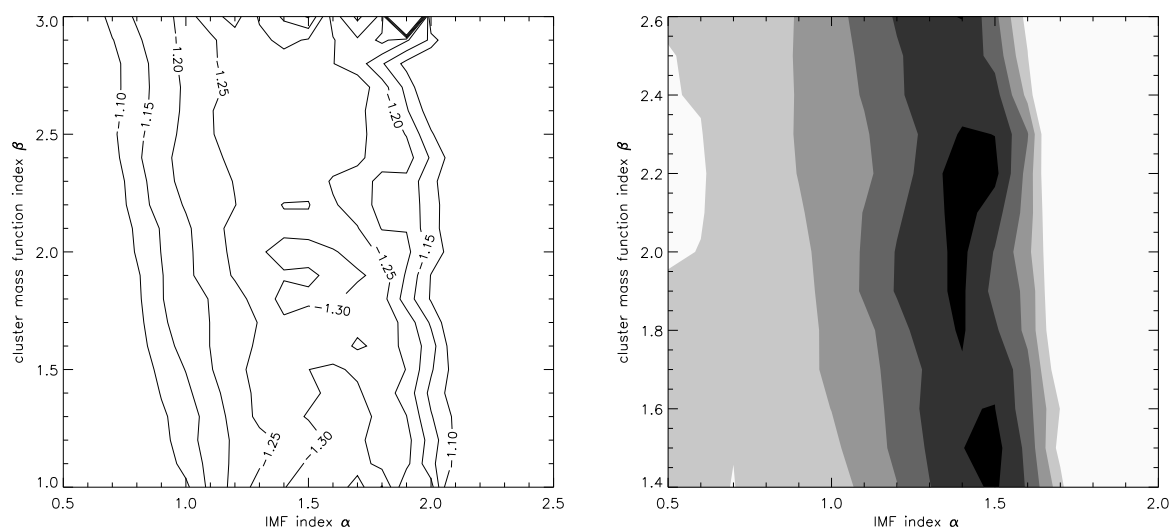


Fig. 9.— The first panel shows the index of a power-law fit to the upper end of a synthetic  $Q$  distribution, as a function of stellar IMF index  $\gamma$  and cluster mass function index  $\beta$ . It is more robust not to impose a power-law on either the observed or model  $Q$  distribution, so confidence contours for the fitting the data with this type of model are shown in the second panel. The data is best fit by the white regions, and the goodness-of-fit decreases with darker shades.

radiation, and there are some that are probably background nonthermal sources. The spectral index of the compact sources detected is often larger (more consistent with thermal radiation or a higher optical depth) than the spectral index calculated for the same source from the relatively low resolution Parkes data. This is expected physically, because the more diffuse emission around a compact embedded source will be optically thin, driving the spectral index from a positive value toward zero. Although most candidates with WC89 infrared colors apparently contain compact H II regions, no obvious trends that more extreme infrared colors indicate more embedded radio sources were seen *at these resolutions*.

We model the total luminosity and Lyman flux ( $Q$ ) distributions of the regions, using a Monte-Carlo method to model those *cluster* number distributions as a function of the *stellar* mass function within a cluster and the cluster number or mass distribution. We find that the population of young clusters in the Magellanic Clouds, as observed through their compact H II regions, is consistent with a stellar IMF that one would find reasonable in the Milky Way: slightly steeper than Salpeter, with a power-law index  $\gamma \simeq 1.5$ . We find that the Magellanic Cloud cluster distribution is consistent with a fairly broad range of cluster mass functions, but the best-fit has a power-law index  $\beta \simeq -2.0$ , which is expected from the mass distribution of interstellar molecular clouds on many scales.

## 5. Acknowledgments

We thank Ed Churchwell for useful discussion. This work would not have been possible without the dedicated work of Robin Wark, Jim Caswell, and the other staff at the Australia Telescope National Facility. R.I. was supported at the start of this investigation by an NSF Graduate Student Fellowship to the University of Colorado, and currently supported by NASA (GLIMPSE *Spitzer* Legacy Grant to E. Churchwell, U. Wisconsin). K.J. is currently supported by an NSF A&AP postdoctoral fellowship. P.C. acknowledges support from NSF (AST 9731570).

The Second Palomar Observatory Sky Survey (POSS-II) was made by the California Institute of Technology with funds from the NSF, NASA, the National Geographic Society, the Sloan Foundation, the Samuel Oschin Foundation, and the Eastman Kodak Corporation. This research made use of the NASA/ IPAC Infrared Science Archive, which is operated by the Jet Propulsion Laboratory, California Institute of Technology, under contract with the National Aeronautics and Space Administration. This research also made extensive use of NASA’s Astrophysics Data System Bibliographic Services, and of the SIMBAD database operated at CDS, Strasbourg, France.

## A. Detections in Individual Regions

### A.1. Small Magellanic Cloud

#### A.1.1. N66

N66 is the brightest H II region in the SMC, and should not be confused with a famous planetary nebula of the same name in the LMC. The region does not appear to have significant atomic (Staveley-Smith et al. 1997) or molecular gas (except for a cloud to the NE, Contursi et al. 2000). Figure 10 shows the POSS-II R image of N66 with important objects marked, including the location of SNR 0057-7226 (Ye, Turtle, & Kennicutt 1991). Interpretation of the region is complicated by the presence of that SNR and the spatially coincident wind-blown bubble from HD5980, which may be behind the SNR (see cartoon of the region in Danforth et al. 2003, Figure 6). The main H II region (elongated to the NW-SE) is likely powered by the cluster NGC 346 visible in Figure 10. Massey, Parker, & Garmany (1989) performed an extensive study of the stellar content of the region, and find several very massive (40–85  $M_{\odot}$ ) stars and many B-type stars. Our radio contours show two compact sources to the southeast of NGC 346.

High-resolution 3 cm radio contours of the northern source (0057-7226) are shown superimposed on H $\alpha$  emission in the third panel of Figure 10. Filamentary structure seen in H $\alpha$  emission is reflected by complex morphology of the radio continuum emission in N66. This source is coincident with the mid-IR peak “H” in Contursi et al. (2000), which they find to have an unremarkable mid-infrared spectrum. The source has complex morphology in both radio continuum and H $\alpha$ . While it does not appear to be associated with any of the stars Massey, Parker, & Garmany (1989) identified as massive (and relatively unembedded) based on U-B color, it is spatially coincident with the emission-line object Lin 350 (Meyssonnier & Azzopardi 1993, who identify it as a compact H II region based on H $\alpha$  spectral line morphology). This radio source also lies within the CO(2-1) contours in the observations of Rubio et al. (2000).

The other source, 0057-7226(S) is also associated with the H II region N66 (as above). However, it does not appear to have a  $7\mu\text{m}$  counterpart in the Contursi et al. (2000) ISOCAM observations, and it does not fall within the CO(2-1) contours of Rubio et al. (2000). In combination with its spectral index ( $\alpha \simeq -0.5$ ), this suggests that it may not be an UCH II region, but perhaps a background object (e.g. AGN), or supernova remnant.

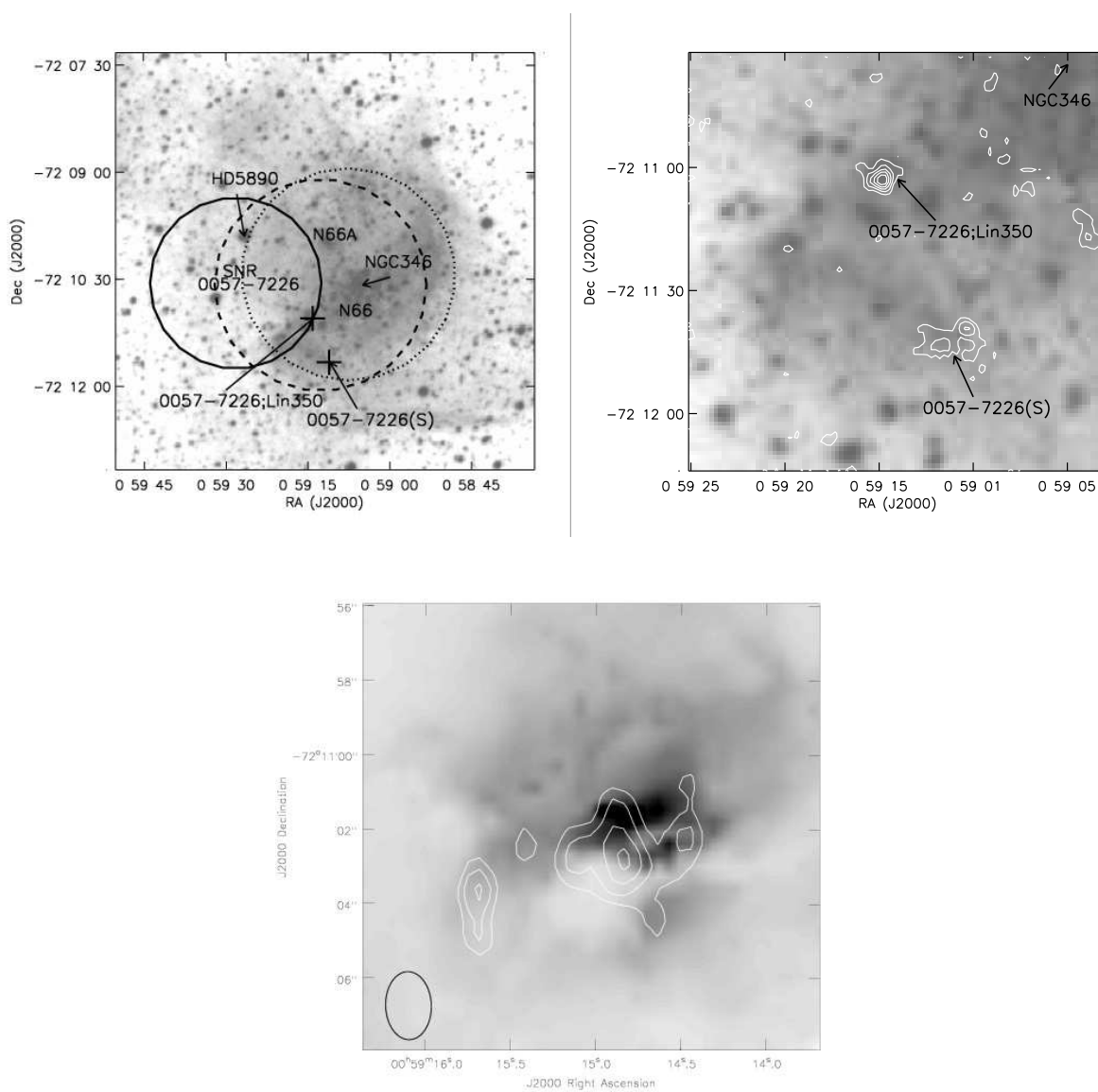


Fig. 10.— Panel 1 is a POSS-II R image of the N66 H II complex, with optically identified subregions labeled. The Parkes 3 and 6 cm source (Filipović, Haynes, White, & Jones 1998) is indicated by the dashed line, and the IRAS point source by the dotted line (where the size of the circle is the spatial resolution of those surveys). The compact radio sources detected in this survey are marked with crosses. The supernova remnant 0057-7226 is marked with a solid circle. The second panel shows 6 cm contours from this dataset on a zoomed-in optical image. The third panel shows contours of 3 cm compact emission superimposed on an *HST* H $\alpha$  image.

### A.1.2. N81 and N88

N81 (DEM 138, IC 1644) and N88 are bright H II regions in the Shapley Wing 1deg.2 SE of the main bar of the SMC. They have two of the highest optical surface brightness and magnitudes among SMC H II regions, and may be located in neighboring and interacting H I clouds (Heydari-Malayeri, Le Bertre, & Magain 1988, and references therein). Figures 11 and 12 show the optical appearance of the two regions, with compact radio sources, IRAS, and Parkes radio sources marked. Radio contours are also shown on zoomed-in optical images. The compactness and apparent simplicity of these two regions make them good candidates for single-generation simple clusters.

The source 0107-7327 is clearly associated with N81. The *HST* observations of Heydari-Malayeri et al. (1999) indicate that N81 is powered by a small group of newly born massive stars. This radio source has also been detected in the CO(1-0) observations of Israel et al. (1993). The sources 0107-7327(N) and 0107-7327(W) are weak detections, but the northern source could also be associated with N81. Similarly, 0122-7324 is clearly associated with N88.

The third panels of Figures 11 and 12 show contours of 3 cm radio emission superimposed on H $\alpha$  images of N81 and N88, respectively. In both cases the radio and optical morphologies agree fairly well. The radio emission from N88A appears to be offset somewhat to the west of the H $\alpha$  emission, although the  $\sim 1''$  pointing uncertainty of *HST* should be kept in mind in interpreting this offset. Heydari-Malayeri et al. (1999) describe the sharp north-western boundary of H $\alpha$  emission as an ionization front, but if the radio emission extends further in that direction, the lack of H $\alpha$  could be an obscuration effect.

Heydari-Malayeri et al. (1999) require  $1.4 \times 10^{49}$  photons  $s^{-1}$  of ionizing radiation to account for the H $\beta$  flux of N81. They estimate the brightest star which they observe in Strömgren  $y$  is consistent with an O6.5V, which would produce sufficient ionizing radiation, but argue convincingly based on their images that the region is powered by a small cluster and not a single star. In N88A, Heydari-Malayeri et al. (1999) find that the average extinction is  $A_v = 1.5$  and rises to values at least as high as 3.5, which is unusual for low metallicity SMC H II regions (see also Kurt et al. 1999). Due to the heavy extinction, the exciting star (or stars) is not detected. Based on the H $\beta$  flux, they estimate a Lyman continuum flux for this object of  $2 \times 10^{49}$  photons  $s^{-1}$ . The Lyman continuum fluxes implied by our radio flux densities for the central sources of N81 and the source in N88A are  $1.3$  and  $3.3 \times 10^{49}$  photons  $s^{-1}$ , respectively. The somewhat higher flux required by the radio observations than the H $\beta$  in N88A is consistent with the high extinction in the area, although the flat radio spectral index indicates that the ionized gas is not itself at remarkably high density.

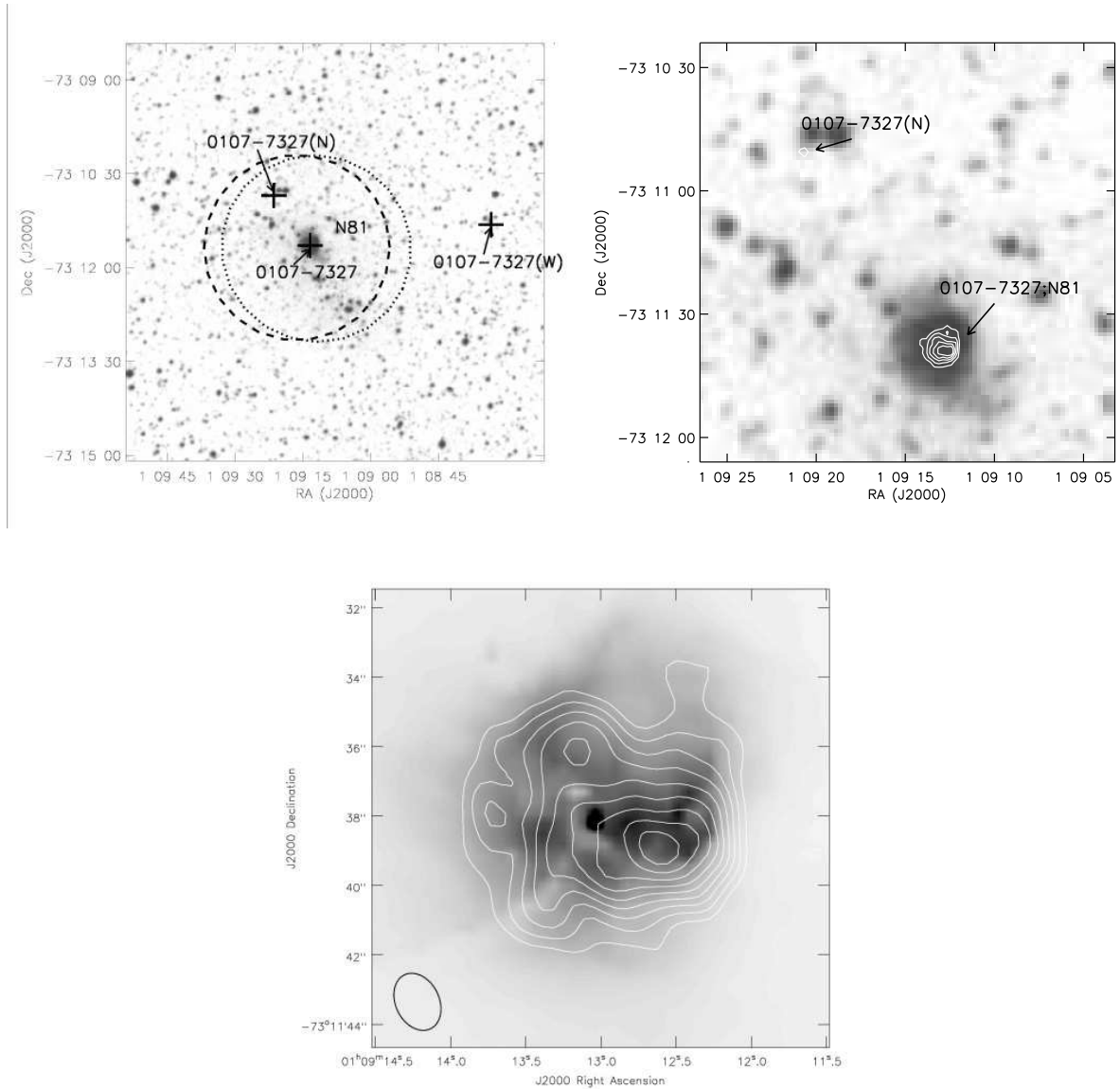


Fig. 11.— The first two panels show POSS-II R images of the N81 H II complex, with optically identified subregions labeled in panel (a). Parkes 3 and 6 cm sources (Filipović, Haynes, White, & Jones 1998) are indicated by dashed lines, and IRAS point sources by dotted lines (with the size of the circle indicating the spatial resolution of those surveys). The compact radio sources detected in this survey are marked with crosses. In the second panel, 6 cm contours are shown on a zoomed-in optical image. The third panel shows contours of high-resolution 3 cm radio emission superimposed on an *HST* H $\alpha$  image.

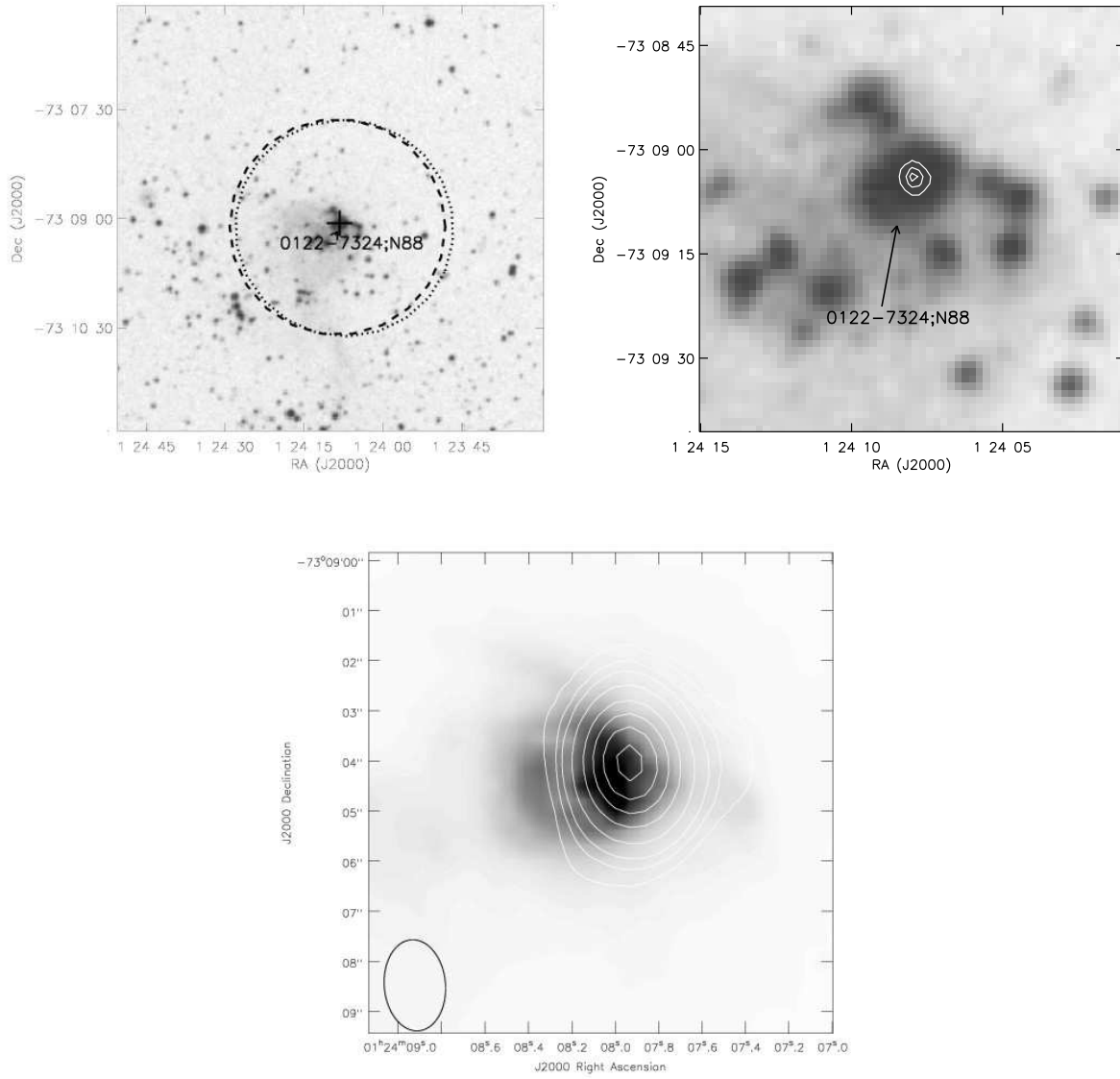


Fig. 12.— The first two panels show POSS-II R images of the N88 H II complex, with subregions labeled as in Figures 10 and 11. The third panel shows contours of high-resolution 3 cm radio emission superimposed on an *HST* H $\alpha$  image.

### A.1.3. N12, N26, N33, & N78

Two sources were detected near H II region N12, but it is not clear that either is directly related to the optical or infrared emission. The source 0043-7321 may be associated with the H II region NGC 249 (N12B). Copetti (1989) estimates that NGC 249 has a Lyman continuum flux of  $\sim 3.2 \times 10^{49} \text{ s}^{-1}$ , and the age of the H II region is  $< 2$  Myr. The source 0043-7321(N) may be associated with the H I shell [SSH97]106. Staveley-Smith et al. (1997) estimate that this H I shell has a radius of  $\sim 4.7'$ , and expansion velocity of  $9.2 \text{ km s}^{-1}$ , and an age of  $5.2$  Myr. For each of the regions N12, N26, N33, and N78, Figure 13 shows a POSS-II R image with important objects labeled following the convention of Figures 10–12, and a zoomed-in image showing our 6 cm radio contours.

The source 0046-7333 is nearest to the H II region N26, but amid a high density of H II regions, including N20, N21, N23, N25, N26, N28, and N12 = DEM 15. This radio source is also near the dark nebulae [H74]11–14 (Hodge 1974) and co-spatial with the molecular cloud SMC B2 (Rubio et al. 1993). Testor (2001) estimates the Lyman continuum flux powering N26 to be  $\sim 2.8 \times 10^{48}$ .

The source 0047-7343 appears to be associated with N33 (Lin 138). 0047-7343(N) may be associated with N31 (DEM 44, Lin 120), which has an optical extent of  $4 \times 7$  arcmin, so is broadly associated with everything in this field. Also nearby is the planetary nebula candidate [JD2002] 7 (Jacoby & De Marco 2002), but as that has a diameter of only  $7''$ , it is probably unrelated.

The sources 0103-7216 and 0103-7216(N) may be associated with the H II region N78 (DEM 126). Copetti (1989) estimates that DEM 126 has a Lyman continuum flux of  $\sim 5 \times 10^{49} \text{ s}^{-1}$ , and the age of the H II region is  $3 - 4$  Myr. The star cluster IC1624 is nearby to the south but apparently unrelated.

## A.2. Large Magellanic Cloud

### A.2.1. N159/N160

The N159/N160 H II region complexes are located  $\sim 40'$  to the south of 30 Doradus, in what appears to be a region in which star formation is propagating from the relatively evolved 30 Dor region out into the more quiescent southern CO arm (Bolatto et al. 2000, and references therein). Figure 14 shows a POSS-II NIR image of the region, in which the main components are visible, and optical H II regions are labeled. The star clusters LH103 and LH105 are  $\gtrsim 5'$  in diameter, and contain the entire N160 and N159 regions, respectively. See



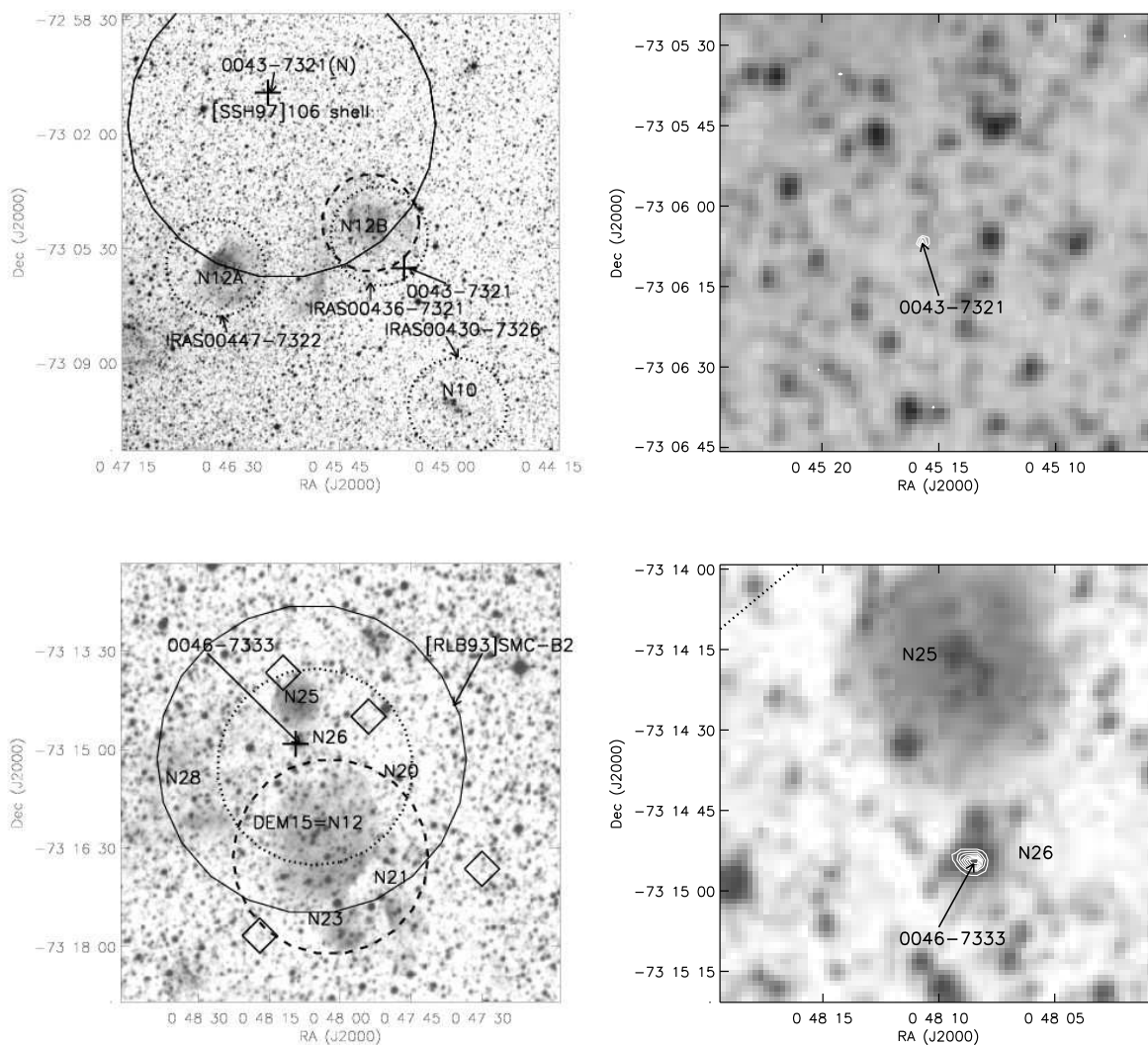


Fig. 13.— Optical images of the N12, N26, N33, and N78 regions with compact sources from this dataset, previously known objects, IRAS and Parkes radio sources marked. Notation as Figure 11. In the first of the two panels showing N26, the large diamonds denote the positions of the dark nebulae [H74]11–14 (numbers are in order of increasing R.A.), presumably associated with dense gas.

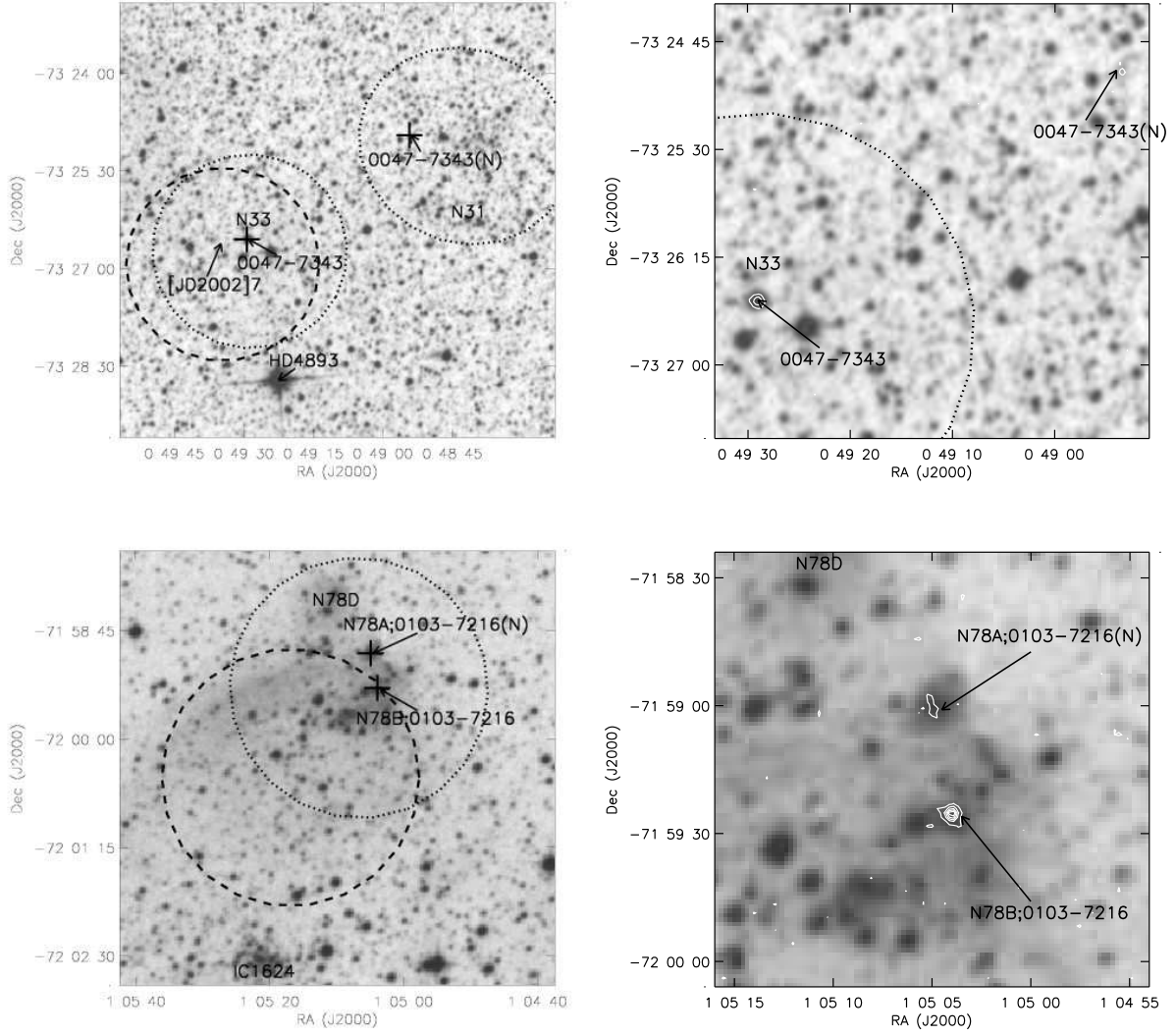


Fig. 13.— continued.

(Bica, Dutra, & Barbuy 2003) for a complete LMC object catalog with sizes and positions. Parkes 3 and 6 cm sources (Filipović, Haynes, White, & Jones 1998) are indicated by dashed lines, and IRAS point sources by dotted lines (with the size of the circle indicating the spatial resolution of those surveys). The compact radio sources detected in this survey are marked with crosses.

In the more evolved N160 region, we detect 5 compact radio sources near the optical H II region N160A. Figure 15 shows our 6 cm contours on a Strömgren  $y$  image taken with *HST* by Heydari-Malayeri et al. (2002). Our source #3 is associated with their H II region N160A1, and they detect a single bright star (their #22) in the vicinity. Similarly, our source #1 is associated with what they denote N160A2, in which they find a small cluster of stars. The authors derive that  $8.5 \times 10^{48}$  photons  $s^{-1}$  and  $1.2 \times 10^{48}$  photons  $s^{-1}$  are required to explain the observed  $H\beta$  fluxes of A1 and A2, respectively, and note that some of the ionizing radiation could come from the cluster between the two, and not just from the apparently associated stars. The ionizing fluxes required to explain our 3 cm flux densities are  $1.4 \pm 0.2 \times 10^{49}$  photons  $s^{-1}$  and  $3.4 \pm 0.2 \times 10^{49}$  photons  $s^{-1}$  for source #3 and #1 (A1 and A2), respectively. These are likely string lower limits to the ionizing flux present in the region, since there is clearly an extended halo of lower-density ionized gas around the two radio sources which is not accounted for in our 3 cm synthesis image flux density. Each of our sources is also detected in the near-infrared by 2MASS – the full infrared and multiwavelength properties of this region are beyond the scope of this survey paper and will be discussed in more detail in a future paper.

The H II region N159 lies to the south; Figure 16 shows a zoomed-in POSS-2 NIR image with our 6 cm contours and important previously identified objects labeled. We detect the compact sources #1, #4, and #5 imaged by Hunt & Whiteoak (1994) using the ATCA at lower resolution ( $\sim 4 \times$  shorter longest baseline, their Figure 1). Their sources #2 and #3 are clearly extended even at their lower resolution, so it is not surprising that there are no compact sources detected at those locations. Hunt & Whiteoak (1994) quote peak intensities at 6 cm for components 1, 4, and 5 as 66, 115, and 58 mJy, respectively. We detect compact sources of 70, 120, and 30 mJy (integrated, though since the sources are at best marginally resolved, the peak flux density/beam is very similar). These numbers indicate that sources #1 and #4 are consistent with unresolved point sources, but that #5 is more diffuse (a fact that is fairly evident in their radio map).

Figure 16 also compares the radio continuum and  $H\alpha$  emission from source #1. The reader should take careful note of nomenclature, as this object is referred to as N159-5 in Heydari-Malayeri et al. (1999) and Meynadier et al. (2004), N159 Blob in Heydari-Malayeri & Testor (1985), and source #1 in Hunt & Whiteoak (1994). The  $H\alpha$  emission imaged

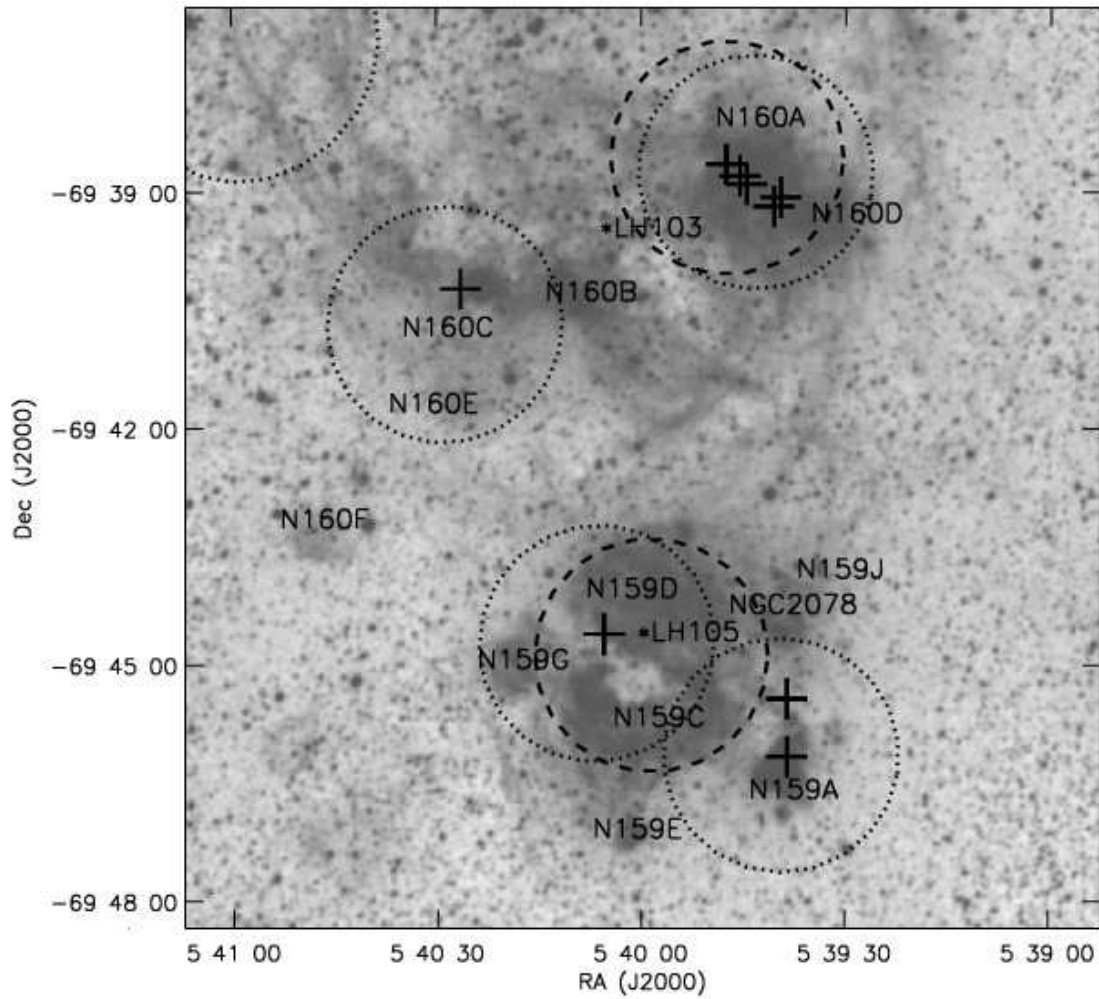


Fig. 14.— POSS-II NIR image of the N159/N160 region, in which the main optical H II regions are labeled. Parkes 3 and 6 cm sources (Filipović, Haynes, White, & Jones 1998) are indicated by dashed lines, and IRAS point sources by dotted lines (with the size of the circle indicating the spatial resolution of those surveys). The compact radio sources detected in this survey are marked with crosses.

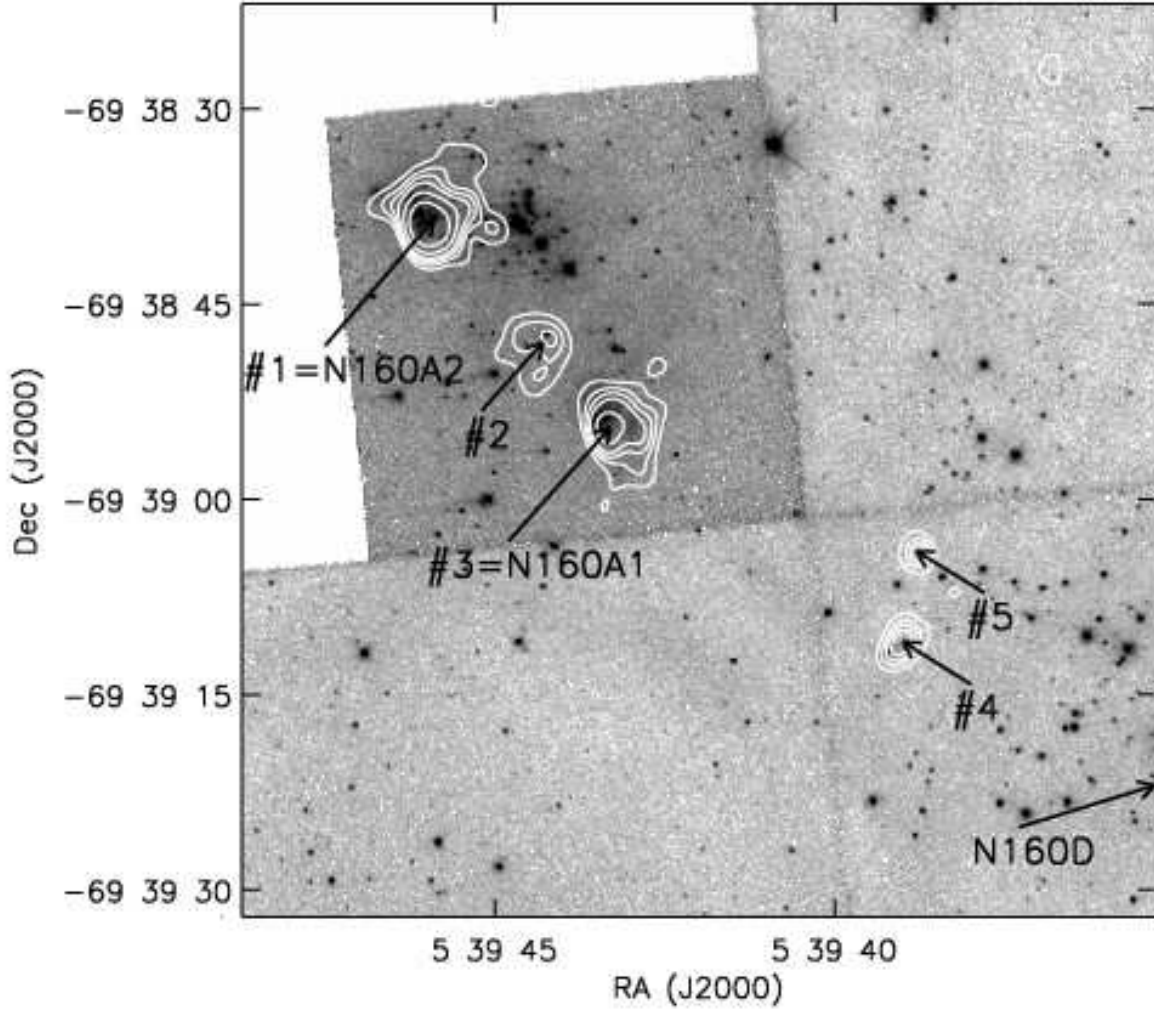


Fig. 15.— N160, imaged at 6cm with the highest-resolution configuration of the ATCA (contours) and in Strömgren *y* (greyscale from *HST*, Heydari-Malayeri et al. 2002).

at high resolution with *HST* (Heydari-Malayeri et al. 1999) shows two lobes, and the new high-resolution radio imaging reveals that most of the radio continuum is associated with the western lobe. Heydari-Malayeri et al. (1999) quote an ionizing flux of  $4 \times 10^{48}$  photons  $\text{s}^{-1}$  if the region is ionization-bounded, but do not postulate any ionizing sources. Our 3 cm flux density corresponds to an ionizing flux of  $9 \times 10^{48}$  photons  $\text{s}^{-1}$ , which could be provided by a single O7-8V star, or more likely a small cluster. A radio-determined ionizing flux will usually exceed an optically-determined one because of extinction, and both are lower limits if ionizing radiation is escaping the H II region or absorbed by dust. Deharveng & Caplan (1992) account for the ionization of the region with the 5 massive stars which they observe in the region, in particular their stars #204 (O5-6V) and #205 (O7-8V), but these stars are at least  $10''$  to the SE of the brightest  $\text{H}\alpha$  and radio region.

### A.2.2. N11

The giant H II complex N11 has the second brightest  $\text{H}\alpha$  luminosity in the LMC, after 30 Dor (Kennicutt & Hodge 1986). The complex consists of numerous H II regions roughly on the edge of a ring or bubble (Rosado et al. 1996, provide a good overview of the region and label the optical subcomponents in their Figure 1). The morphology probably results from (at least) two generations of star formation, the older ( $\sim 5 \times 10^6$  yr Walborn & Parker 1992) being the central OB association LH9, with younger associations including LH10 ( $1-2 \times 10^6$  years old) on the periphery. Figure 17 shows the region with optical H II regions labeled, as well as Filipovic and our radio sources and IRAS point sources. The older cluster LH9 is clearly visible in the center of the ring of H II regions delineated by N11A,B,C,F, and H (just off the image to the west).

We detect compact sources in the two highest excitation regions A and B (“excitation” refers to the ratio of  $[\text{O III}]\lambda 5007/\text{H}\beta$  and is probably related to the hardness of the powering radiation field: Heydari-Malayeri et al. 2001, and references therein). Figure 18 shows 3 cm high-resolution radio contours of 0456-6629(E) superimposed on *HST*  $\text{H}\alpha$  of N11A. The radio and  $\text{H}\alpha$  morphologies of N11A agree very well, supporting the interpretation that the H II region is less extended from the ionizing stars to the north-east because of the presence of a dense molecular cloud (Heydari-Malayeri et al. 2001). The  $\text{H}\alpha$  morphology could have been highly affected by extinguishing material, but the unextinguished radio emission confirms the lack of ionized gas to the NE. The second panel of Figure 18 shows the western of two sources detected in N11B, 0456-6629(W2). The source is in the region of brightest  $\text{H}\alpha$  emission, on the northeast side of what appears to be the powering star cluster. Interestingly, the radio continuum source is located in the middle of ring-like  $\text{H}\alpha$  emission. The complex  $\text{H}\alpha$

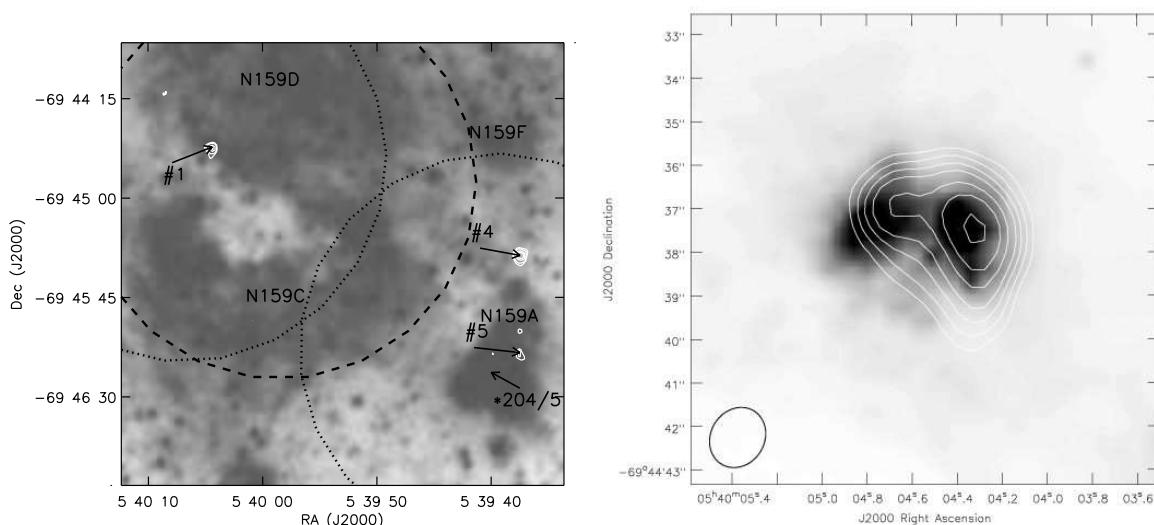


Fig. 16.— The first panel shows a POSS-2 NIR gray-scale image of the N159 region, with our 6 cm radio contours overlaid, showing detections of Hunt & Whiteoak (1994) sources #1, #4, #5. Also noted are optically identified H II regions, and IRAS and Parkes sources (large circles as in Fig. 10). The position of Deharveng & Caplan (1992) stars #204 and #205, which the authors say are likely major ionizing sources in the region, are labeled “\*204/5”. The second panel shows a close-up of source #1, the “Papillon” nebula (Heydari-Malayeri et al. 1999). 3 cm contours (2, 3, 4, 5, 6.5, 8, and 10 mJy) are overlaid on a narrow-band H $\alpha$  (*HST* WFPC2 F656N) image. Since the H II region was on the edge of our beam, radio contours are from archival (C868) data.

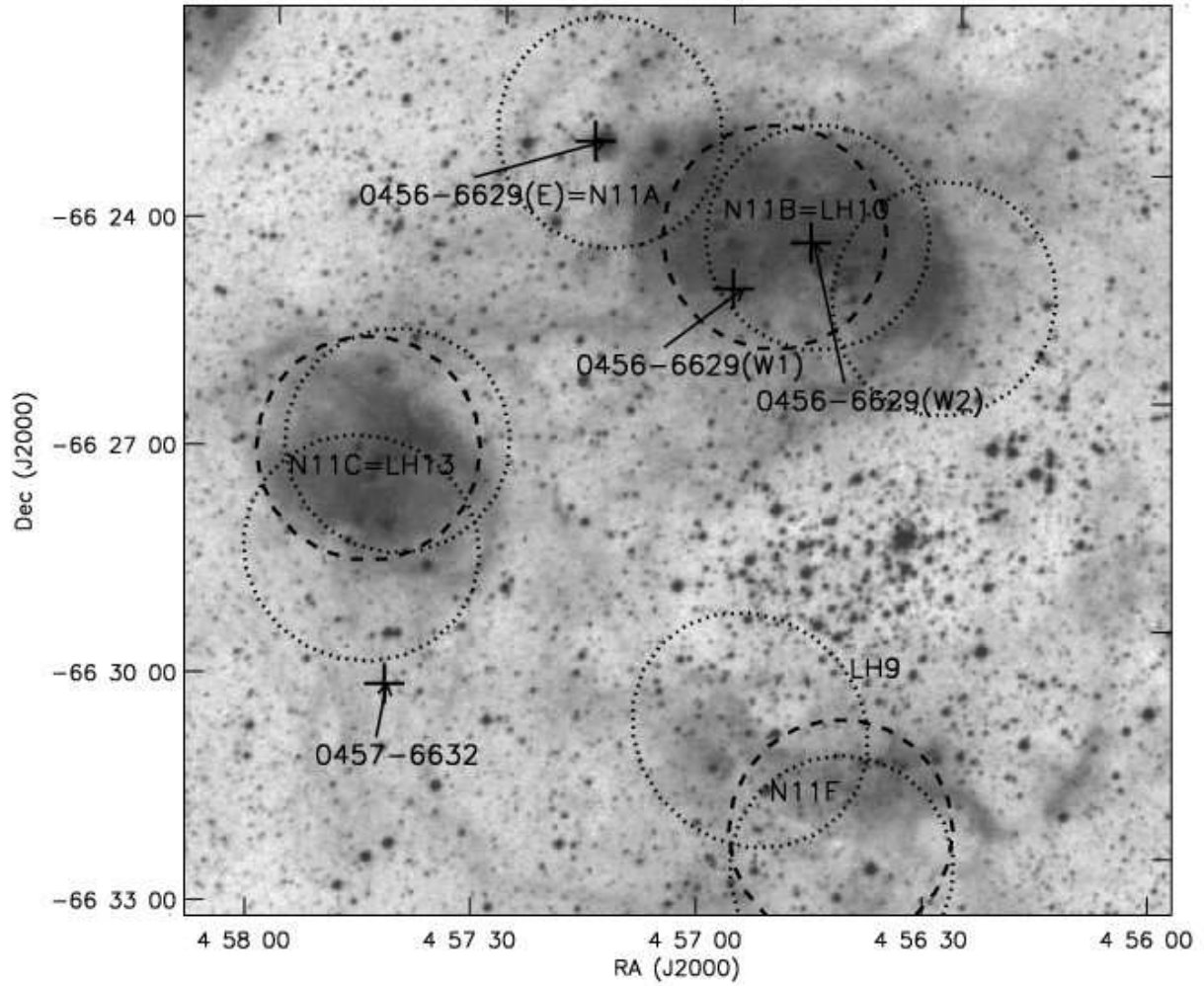


Fig. 17.— POSS-II R image of the N11 H II complex, with optically identified subregions labeled. Parkes 3 and 6 cm sources (Filipović, Haynes, White, & Jones 1998) are indicated by dashed lines, and IRAS point sources by dotted lines (with the size of the circle indicating the spatial resolution of those surveys). The compact radio sources detected in this survey are marked with crosses.



and radio morphology indicates that the nearby material is probably inhomogeneous and clumpy, leading not only to variable extinction of the optical light but an irregularly-shaped H II region. A second source, 0456-6629(W1) was detected to the east of (W2), but still in N11B. The radio source is point-like or unresolved, and is located very close to stars #3189 and #3193 of the extensive study of Parker, Garmany, Massey, & Walborn (1992). The authors unfortunately do not have spectra of these two stars, but they are fairly blue (U-B = -0.9).

*A.2.3. N79, N4, N5, N83, N23, N105, N119, N44, N138, N206, N55, N213, N158, N214, & N168*

Figures 19-29 show the locations of the rest of the LMC compact radio sources relative to nearby optically identified H II regions. In many cases, the compact radio source is not associated with the brightest optical emission. In some but not all cases, the radio emission is more similar to infrared. Many of these regions are relatively unstudied, but we describe the radio sources in as much context as possible with a literature search:

The compact radio emission from Parkes source 0452-6927 is probably related to optical H II region N79B. Figure 19 shows the main compact source, and a fringe of fainter emission to the east.

The N4 region in the north-west part of the LMC consists of two main optical H II regions, with a molecular cloud detected in CO between them (Heydari-Malayeri & Lecavelier Des Etangs 1994). The southern and brighter region (A) has higher excitation ( $H\beta/H\alpha$ ) and higher  $H\alpha$  surface brightness on the NE side, toward the molecular cloud, supporting a classical “champagne flow” model of the H II region. We detect two compact radio sources on that more embedded side of the optical emission (Fig. 20). The brighter radio source 0452-5700(SW) is in the optical emission, and apparently represents the densest ionized gas near the two ionizing sources. The fainter source 0452-6700(NE) is off the edge of the optical emission, and could be a young deeply embedded source in the cloud. Heydari-Malayeri & Lecavelier Des Etangs (1994) require  $3 \times 10^{49}$  photons  $s^{-1}$  to account for the optical hydrogen recombination line flux. The flux density of our brighter radio source requires  $1.3 \times 10^{49}$  photons  $s^{-1}$ , but the optical emission clearly comes from a larger region of ionized gas resolved out in our high resolution observations.

Figure 21 shows the two sources possibly related to Parkes source 0452-6722 and optical H II region N5.

We detect two compact sources associated near the optical H II region N83 (Fig. 22).

0454-6916(E) is coincident with the “high-excitation blob” N83B (Heydari-Malayeri, van Drom, & Leisy 1990), the eastern of several optical H II regions. As with N4, the molecular gas detected in CO peaks on the NE side of the complex (Bolatto, Leroy, Israel, & Jackson 2003, Figure 1), so the higher excitation optical H II region is associated with denser molecular gas *and* a compact radio continuum source. Heydari-Malayeri, van Drom, & Leisy (1990) calculate a required Lyman continuum flux of  $0.75 \times 10^{49}$  photons  $s^{-1}$  to power the H $\beta$  nebula, and we require  $1.1 \times 10^{49}$  photons  $s^{-1}$  to account for the 3 cm radio continuum flux density. The second, much fainter compact radio source 0454-6916(W) is located in a region with little optical emission between two optical H II regions.

Figure 23 shows the two sources possibly related to Parkes source 0505-6807 and optical H II region N23. Nearby objects include a supernova remnant, which is its own Parkes radio source, and a Lucke & Hodge star cluster.

We detect a cluster of 4 compact radio sources near the center of N105 (Fig. 24), an H II region associated with at least 18 OB stars, 2 WR stars, and bright [O III] emission (Ambrocio-Cruz et al. 1998, and references therein). The compact radio sources are in the highest excitation part of the optical nebula, just to the west of the WRC5+O star Brey 16a, in a region associated with masers and a proposed IR protostar.

We detect compact radio sources associated with several of the brighter optical H II regions in the N44 complex (C, D, G and M), around the edges of an H I shell possibly associated with a superbubble (Kim, Chu, Staveley-Smith, & Smith 1998). In N44M, Nazé et al. (2002) quote an ionizing flux of  $1.5\text{--}2.1 \times 10^{48}$  photons  $s^{-1}$  to account for the H $\alpha$  flux, and we need  $2.8 \times 10^{48}$  photons  $s^{-1}$  to account for the 3 cm flux density of 0523-6806(NE). (Oey & Massey 1995) find many OB stars in the N44C region, but without coordinates no particular association with radio source 0522-6800 can be made.

Figure 26 shows the sources near Parkes source 0519-6916 and optical H II region N119, and near Parkes source 0525-6831 and optical H II region N138. Figure 27 shows the sources near Parkes source 0531-7106 and optical H II region N206, near Parkes source 0532-6629 and optical H II region N55, and near Parkes source 0538-7042 and optical H II region N213.

The sources 0539-6931(1) and 0539-6931(2) (Fig. 28) are located in the optical H II region N158C, very near several identified OB stars (Testor & Niemela 1998). Source #1 is near identified O7V and O9V stars, and source #2 is near an identified B0V star. The Lyman continuum fluxes required by the 3 cm measurements are  $3 \times 10^{48}$  and  $1 \times 10^{48}$  photons  $s^{-1}$  for sources #1 and #2, respectively, consistent with single O7.5V–O8V and O9V stars.

Finally, Figure 29 shows the sources near Parkes source 0542-7121 and optical H II region N214, and near Parkes source 0545-6947 and optical H II region N168.

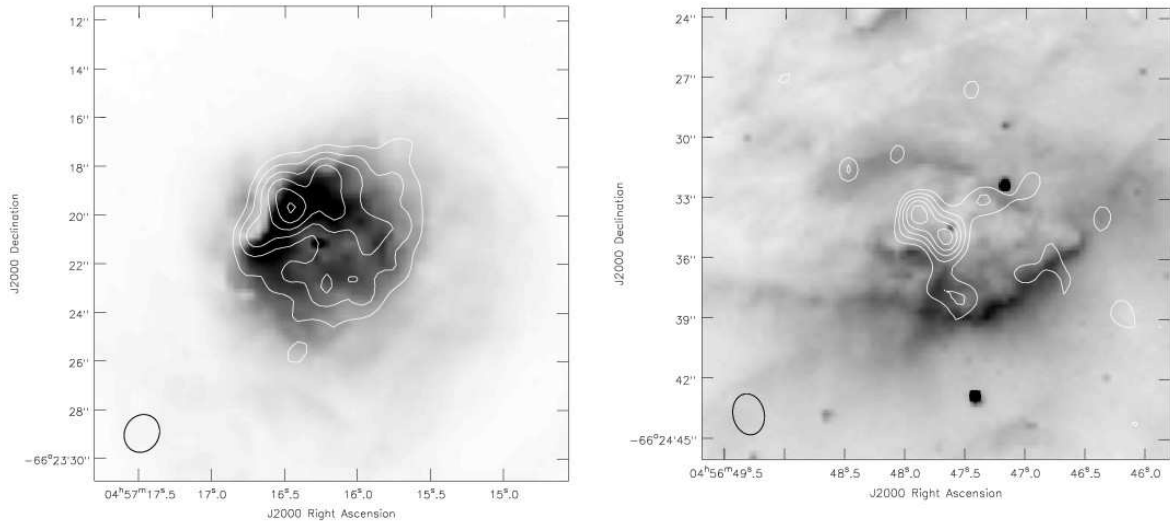


Fig. 18.— The first panel shows 3cm contours (0.7, 1.2, 1.6, 2.1, 2.5 mJy) of N11A, and the second panel shows 6cm contours (0.6, 0.8, 1.0, 1.2, 1.4 mJy) of N11B. Both are overlaid on narrow-band H $\alpha$  (*HST* WFPC2 F656N) images. Since the H II region was on the edge of our 3 cm beam, the 3 cm contours of N11A are from archival (C868) data.

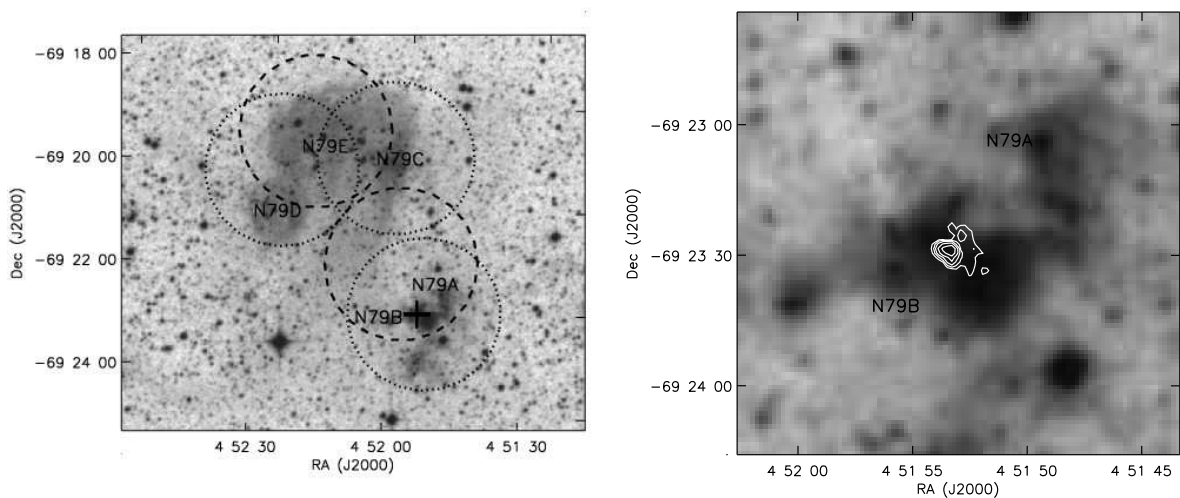


Fig. 19.— Compact sources related to Parkes source B0452-6927 and optical H II region N79 in the LMC. In this and the following figures, each panel is a gray-scale POSS-II R image. In the first of each pair of panels corresponding to a particular region, the locations of the radio sources detected by this study are marked with crosses, as well as important optical nebulae, Parkes radio sources (dashed lines) and IRAS sources (dotted lines), following the convention of previous figures. The second panel of each pair is a zoomed-in version showing our 6 cm radio contours.

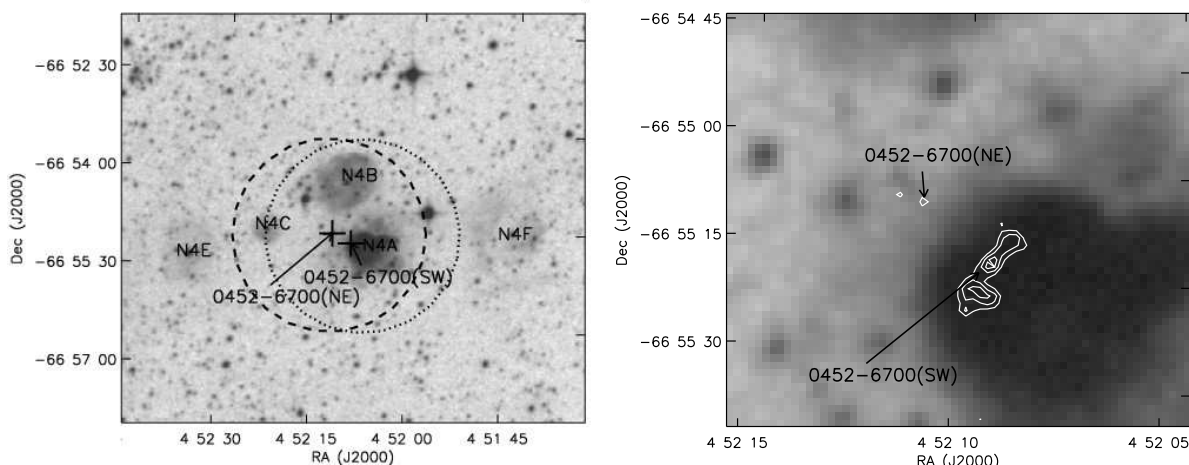


Fig. 20.— Compact sources related to Parkes source B0452-6700 and optical H II region N4, labelled as Figure 19.

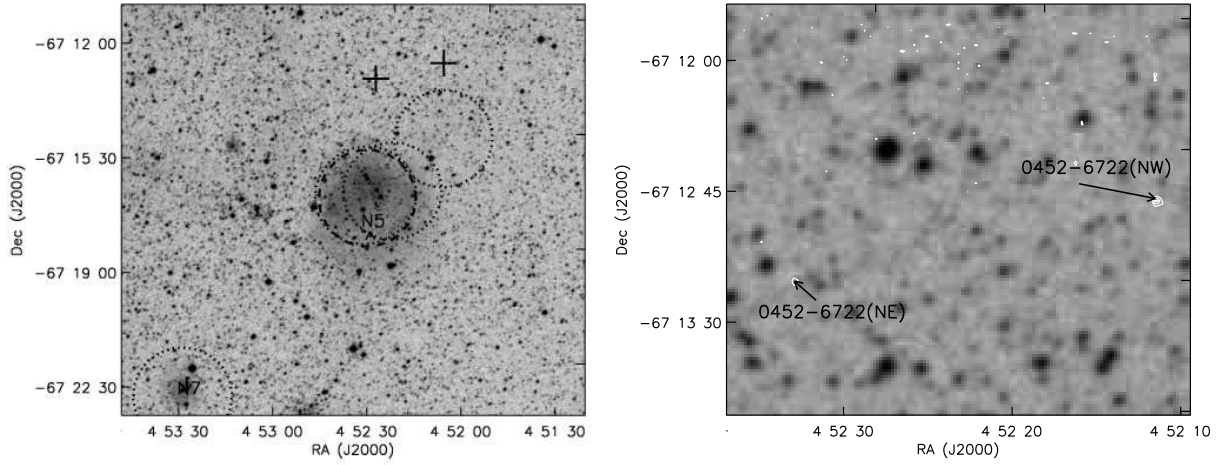


Fig. 21.— Compact sources related to Parkes source B0452-6722 and optical H II region N5, labelled as Figure 19.

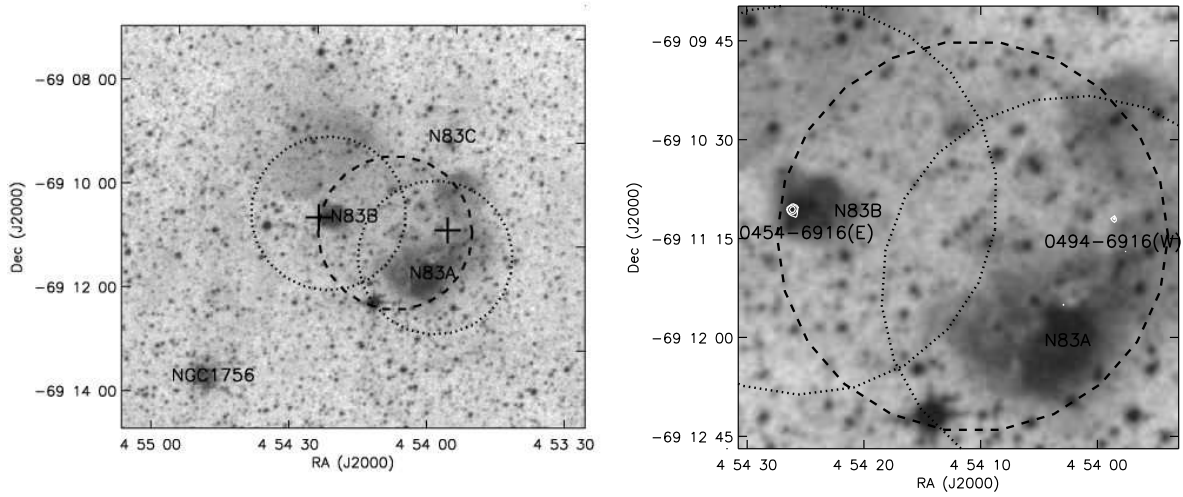


Fig. 22.— Compact sources related to Parkes source B0454-6916 and optical H II region N83, labelled as Figure 19.

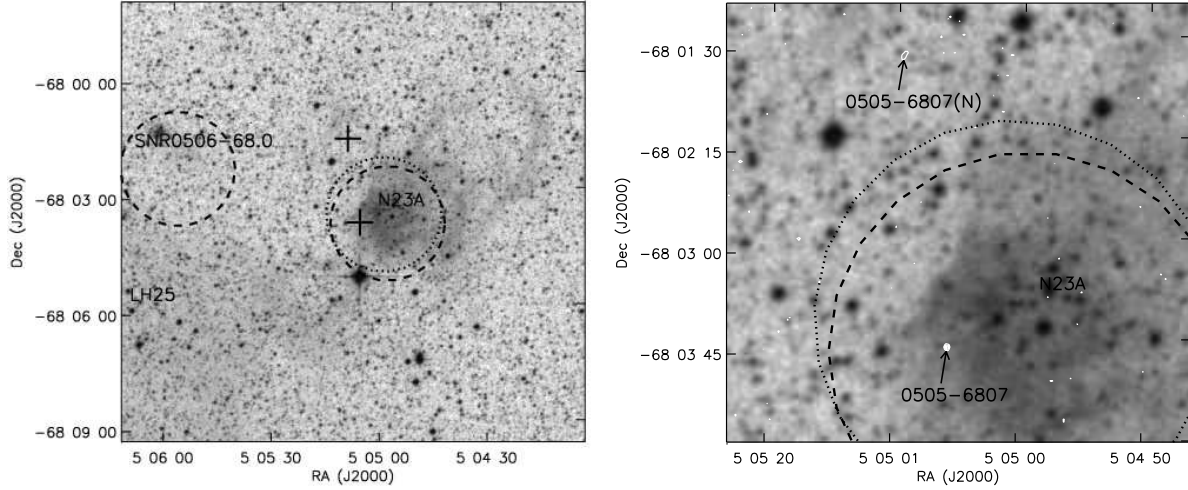


Fig. 23.— Compact sources related to Parkes source B0505-6807 and optical H II region N23, labelled as Figure 19.

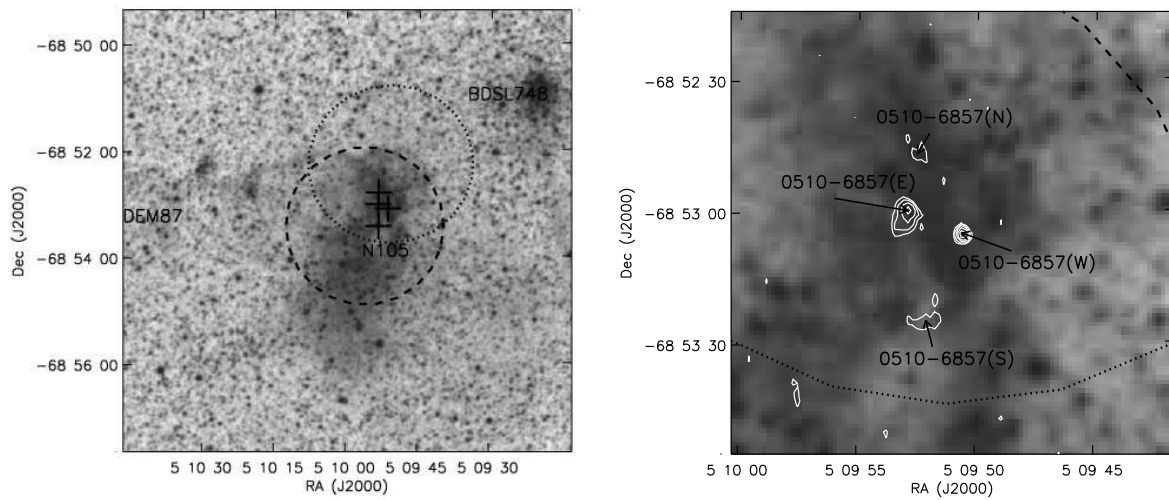


Fig. 24.— Compact sources related to Parkes source B0510-6857 and optical H II region N105, labelled as Figure 19.

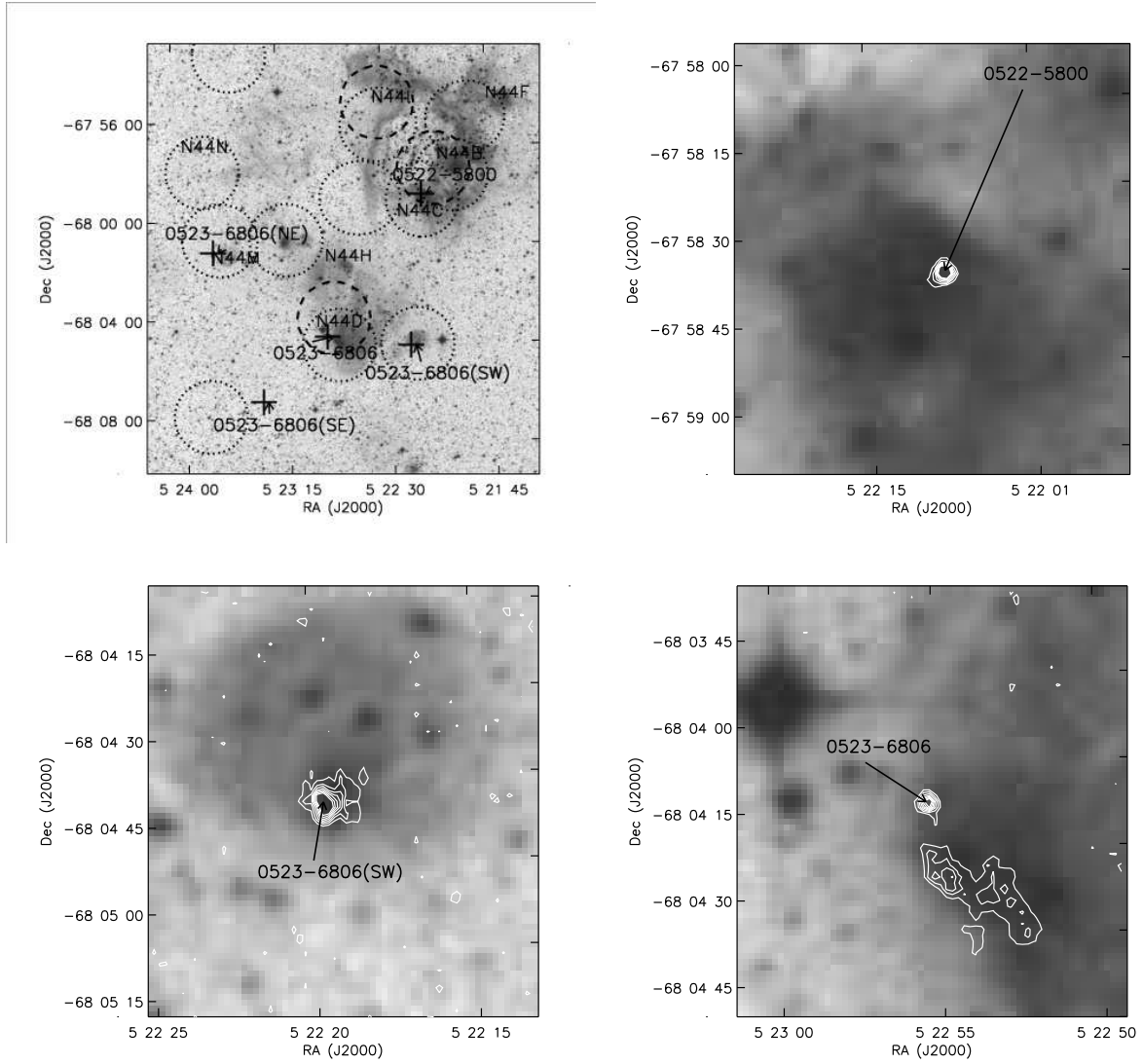


Fig. 25.— Compact sources related to Parkes source B0523-6808 and optical H II region N44, labelled as Figure 19. Zoomed-in images of three different sources in N44 are shown.

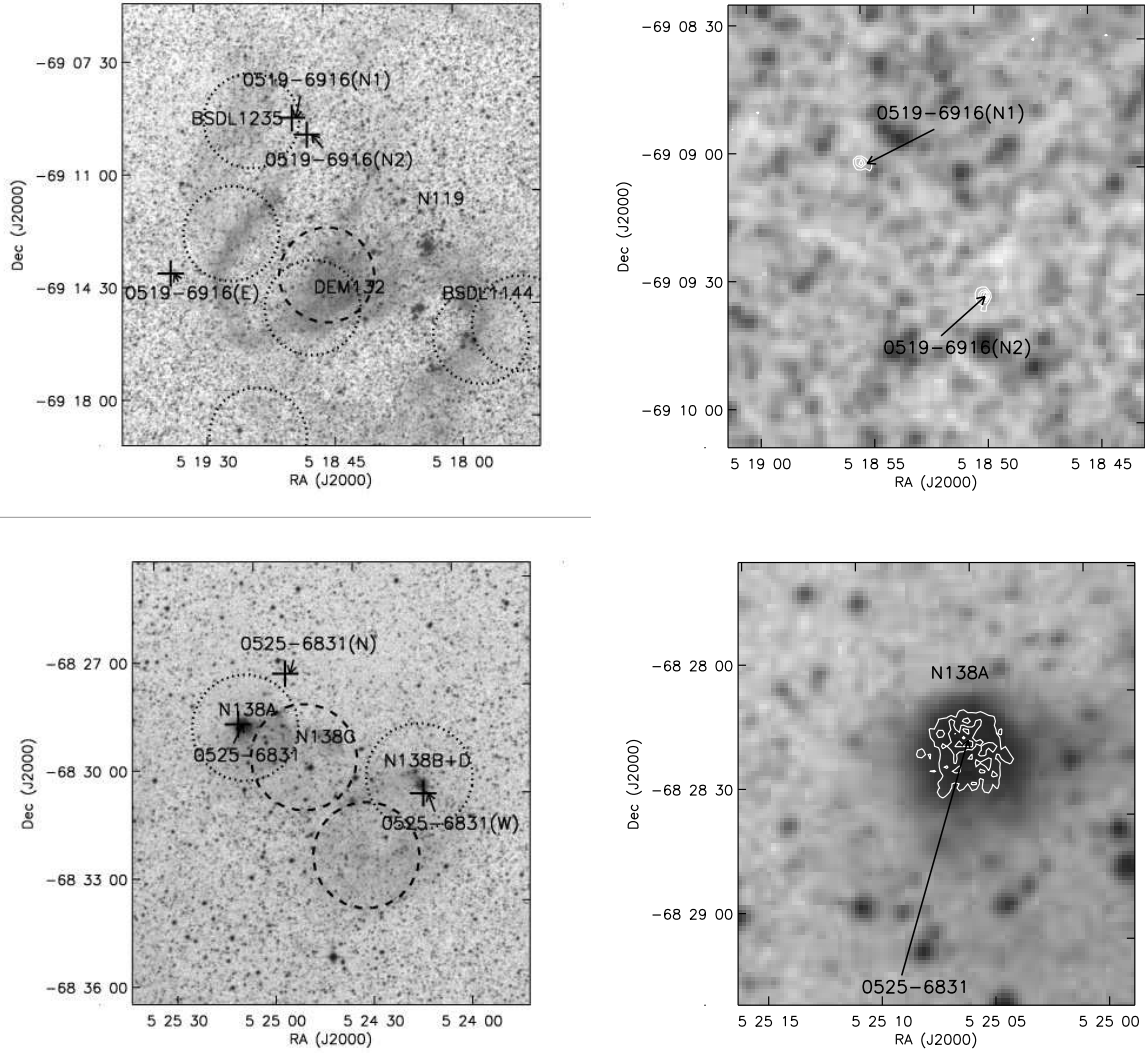


Fig. 26.— Compact sources near Parkes source 0519-6916 and optical H II region N119, and near Parkes source 0525-6831 and optical H II region N138.



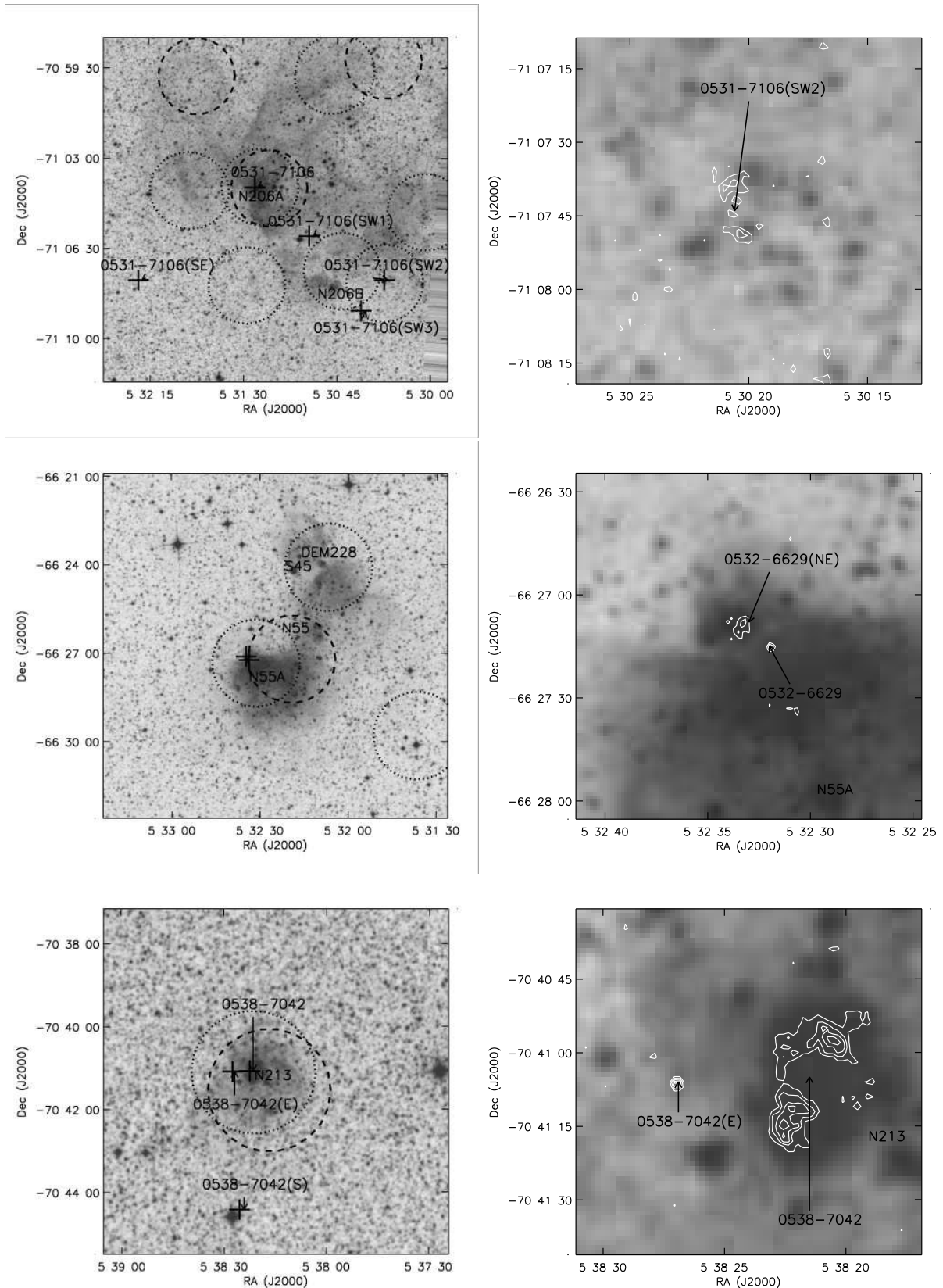


Fig. 27.— Compact sources near Parkes source 0531-7106 and optical H II region N206, near Parkes source 0532-6629 and optical H II region N55, and near Parkes source 0538-7042 and optical H II region N213. Labels as Fig. 19.

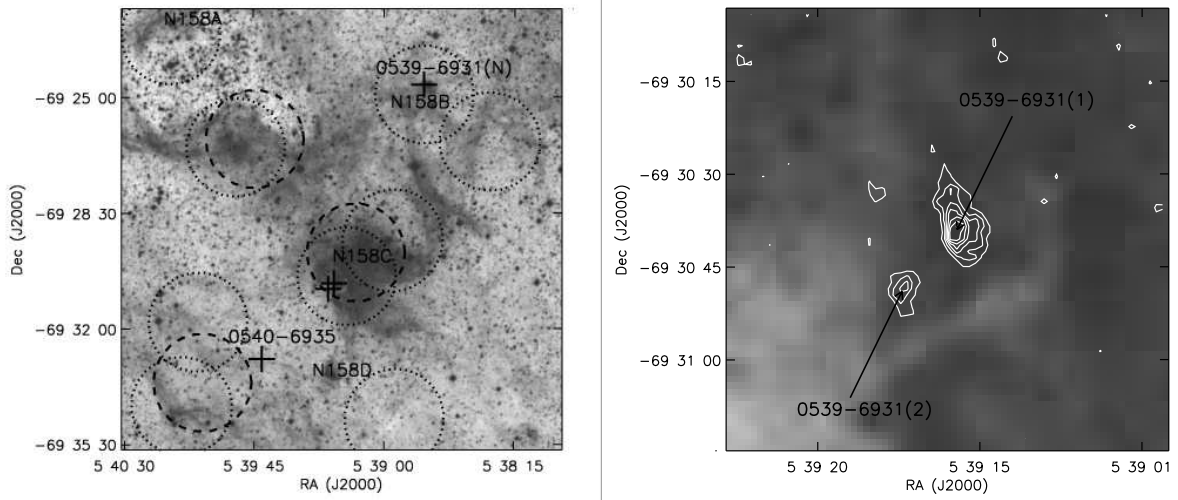


Fig. 28.— Compact sources related to Parkes source B0539-6931 and optical H II region N158, labelled as Figure 19.

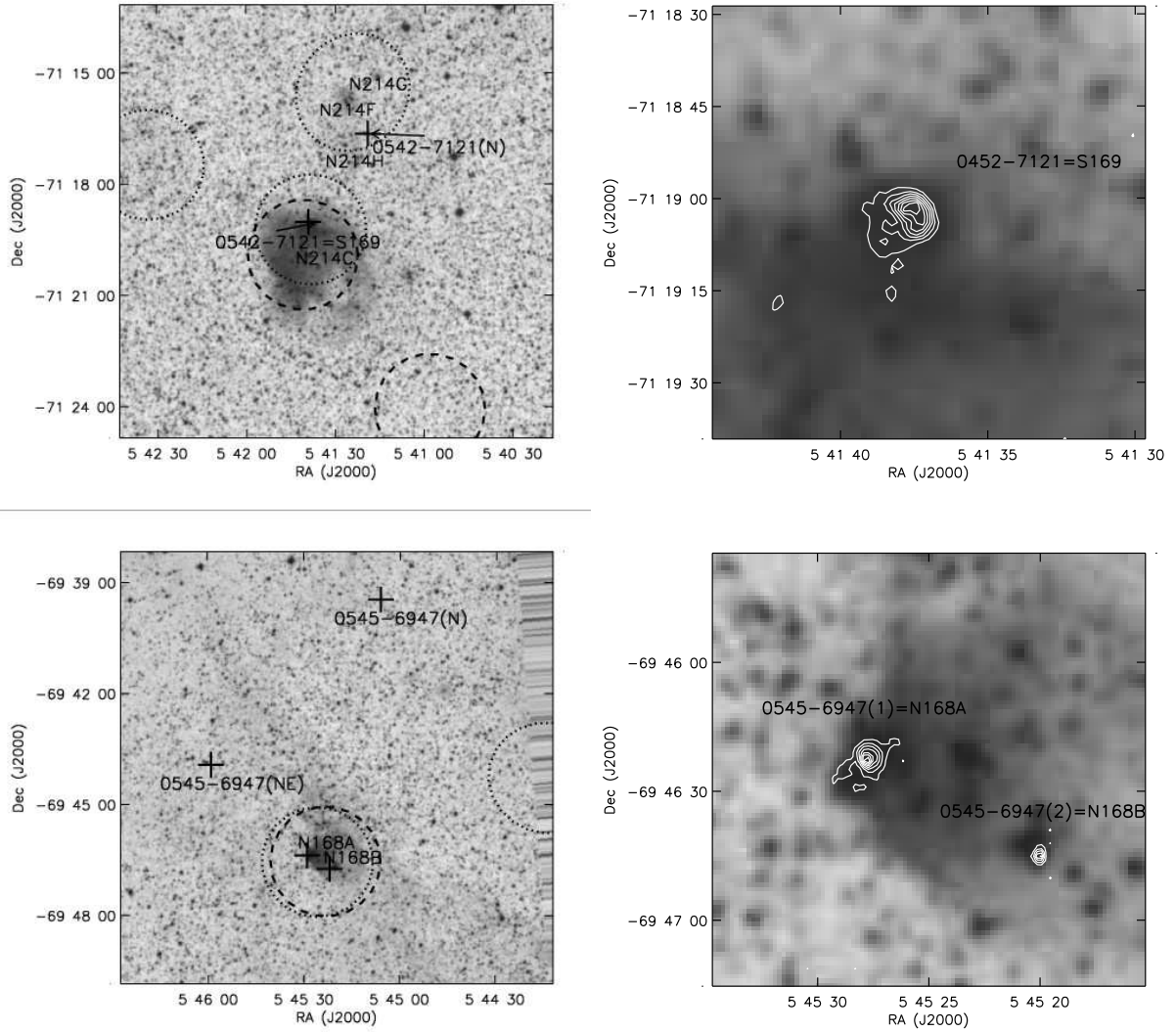


Fig. 29.— Compact sources near Parkes source 0542-7121 and optical H II region N214, and near Parkes source 0545-6947 and optical H II region N168. Labels as Figure 19.

## REFERENCES

- Alonso-Herrero, A. & Knapen, J. H. 2001, *AJ*, 122, 1350
- Alcock, C. et al. 2003, *ApJ*, accepted (astro-ph 0310281)
- Ambrocio-Cruz, P., Laval, A., Marcelin, M., Amram, P., & Comeron, F. 1998, *A&A*, 339, 173
- Beckman, J. E., Rozas, M., Zurita, A., Watson, R. A., & Knapen, J. H. 2000, *AJ*, 119, 2728
- Bica, E., Dutra, C. M., & Barbuy, B. 2003, *A&A*, 397, 177
- Bolatto, A. D., Leroy, A., Israel, F. P., & Jackson, J. M. 2003, *ApJ*, 595, 167
- Bolatto, A. D., Jackson, J. M., Israel, F. P., Zhang, X., & Kim, S. 2000, *ApJ*, 545, 234
- Casassus, S., Bronfman, L., May, J., & Nyman, L.-Å. 2000, *A&A*, 358, 514
- Condon, J. J. 1992, *ARA&A*, 30, 575
- Condon, J. J. 1974, *ApJ*, 188, 279
- Contursi, A. et al. 2000, *A&A*, 362, 310
- Copetti, M. V. F. 1989, *Ap&SS*, 156, 103
- Danforth, C. W., Sankrit, R., Blair, W. P., Howk, J. C., & Chu, Y. 2003, *ApJ*, 586, 1179
- Deharveng, L. & Caplan, J. 1992, *A&A*, 259, 480
- Elmegreen, B. G. & Efremov, Y. N. 1997, *ApJ*, 480, 235
- Filipović, M. D., Haynes, R. F., White, G. L., Jones, P. A., Klein, U., Wielebinski, R. 1995, *A&AS*, 111, 311
- Filipović, M. D., Haynes, R. F., White, G. L., & Jones, P. A. 1998, *A&AS*, 130, 421
- Filipović, M. D., Bohlsen, T., Reid, W., Staveley-Smith, L., Jones, P. A., Nohejl, K., & Goldstein, G. 2002, *MNRAS*, 335, 1085
- Graczyk, D. 2003, *MNRAS*, 342, 1334
- Henize, K. G. 1956, *ApJS*, 2, 315
- Heydari-Malayeri, M., Charmandaris, V., Deharveng, L., Meynadier, F., Rosa, M. R., Schaerer, D., & Zinnecker, H. 2002, *A&A*, 381, 941
- Heydari-Malayeri, M., Charmandaris, V., Deharveng, L., Rosa, M. R., Schaerer, D., & Zinnecker, H. 2001, *A&A*, 372, 527
- Heydari-Malayeri, M., Charmandaris, V., Deharveng, L., Rosa, M. R., & Zinnecker, H. 1999, *A&A*, 347, 841
- Heydari-Malayeri, M., Rosa, M. R., Charmandaris, V., Deharveng, L., & Zinnecker, H. 1999, *A&A*, 352, 665
- Heydari-Malayeri, M., Rosa, M. R., Zinnecker, H., Deharveng, L., & Charmandaris, V. 1999, *A&A*, 344, 848
- Heydari-Malayeri, M. & Lecavelier Des Etangs, A. 1994, *A&A*, 291, 960
- Heydari-Malayeri, M., van Drom, E., & Leisy, P. 1990, *A&A*, 240, 481
- Heydari-Malayeri, M., Le Bertre, T., & Magain, P. 1988, *A&A*, 195, 230
- Heydari-Malayeri, M. & Testor, G. 1985, *A&A*, 144, 98
- Hunt, M. R. & Whiteoak, J. B. 1994, *Proceedings of the Astronomical Society of Australia*, 11, 68
- Hodge, P. W. 1974, *PASP*, 86, 263
- Israel, F. P. et al. 1993, *A&A*, 276, 25

- Jacoby, G. H. & De Marco, O. 2002, *AJ*, 123, 269
- Kennicutt, R. C., Edgar, B. K., & Hodge, P. W. 1989, *ApJ*, 337, 761
- Kennicutt, R. C. & Hodge, P. W. 1986, *ApJ*, 306, 130
- Kim, S., Chu, Y., Staveley-Smith, L., & Smith, R. C. 1998, *ApJ*, 503, 729
- Kurt, C. M., Dufour, R. J., Garnett, D. R., Skillman, E. D., Mathis, J. S., Peimbert, M., Torres-Peimbert, S., & Ruiz, M.-T. 1999, *ApJ*, 518, 246
- Larsen, S. S. 2002, *AJ*, 124, 1393
- Massey, P., Parker, J. W., & Garmany, C. D. 1989, *AJ*, 98, 1305
- McKee, C. F. & Williams, J. P. 1997, *ApJ*, 476, 144
- Meynadier, F., Heydari-Malayeri, M., Deharveng, L., Charmandaris, V., Bertre, T. L., Rosa, M. R., Schaerer, D., & Zinnecker, H. 2004, *ArXiv Astrophysics e-prints*, astro-ph/0403626
- Meyssonier, N. & Azzopardi, M. 1993, *A&AS*, 102, 451
- Nazé, Y., Chu, Y., Guerrero, M. A., Oey, M. S., Gruendl, R. A., & Smith, R. C. 2002, *AJ*, 124, 3325
- Oey, M. S. & Massey, P. 1995, *ApJ*, 452, 210
- Oey, M. S. & Clarke, C. J. 1998, *AJ*, 115, 1543
- Parker, J. W., Garmany, C. D., Massey, P., & Walborn, N. R. 1992, *AJ*, 103, 1205
- Rosado, M., Laval, A., Le Coarer, E., Georgelin, Y. P., Amram, P., Marcelin, M., Goldes, G., & Gach, J. L. 1996, *A&A*, 308, 588
- Rubio, M. et al. 1993, *A&A*, 271, 1
- Rubio, M., Contursi, A., Lequeux, J., Probst, R., Barbá, R., Boulanger, F., Cesarsky, D., & Maoli, R. 2000, *A&A*, 359, 1139
- Smith, L. J., Norris, R. P. F., & Crowther, P. A. 2002, *MNRAS*, 337, 1309
- Staveley-Smith, L., Sault, R. J., Hatzidimitriou, D., Kesteven, M. J., & McConnell, D. 1997, *MNRAS*, 289, 225
- Testor, G. 2001, *A&A*, 372, 667
- Testor, G. & Niemela, V. 1998, *A&AS*, 130, 527
- Vacca, W. D., Garmany, C. D., & Shull, J. M. 1996, *ApJ*, 460, 914
- Walborn, N. R. & Parker, J. W. 1992, *ApJ*, 399, L87
- Wood, D.O. & Churchwell, E. 1989, *ApJS*, 69, 831
- Wood, D. O. S. & Churchwell, E. 1989, *ApJ*, 340, 265
- Ye, T., Turtle, A. J., & Kennicutt, R. C. 1991, *MNRAS*, 249, 722